International Journal of Solids and Structures 51 (2014) 2964–2978

Contents lists available at ScienceDirect

International Journal of Solids and Structures

journal homepage: www.elsevier.com/locate/ijsolstr

A nonlinear finite element model for the stress analysis of soft solids with a growing mass

Yin Liu, Hongwu Zhang *, Yonggang Zheng, Sheng Zhang, Biaosong Chen

State Key Laboratory of Structural Analysis for Industrial Equipment, Department of Engineering Mechanics, Faculty of Vehicle Engineering and Mechanics, Dalian University of Technology, Dalian 116024, PR China

ARTICLE INFO

Article history:
Received 25 December 2013
Received in revised form 20 March 2014
Available online 24 April 2014

Keywords:
Mass growth
Finite element method
Soft material
Multiplicative decomposition
Free growth

ABSTRACT

The paper presents a new finite element (FE) model for the stress analysis of soft solids with a growing mass based on the work of Lubarda and Hoger (2002). Contrary to the traditional numerical methods emphasizing on the influence of growth on constitutive equations, an equivalent body force is firstly detected, which is resulted from the linearization of the nonlinear equation and acts as the driver for material growth in the numerical aspect. In the algorithm, only minor correction on the traditional tangent modulus is needed to take the growth effects into consideration and its objectivity could be guaranteed comparing with the traditional method. To solve the resulted equation in time domain, both explicit and implicit integration algorithms are developed, where the growth tensor is updated as an internal variable of Gauss point. The explicit updating scheme shows higher efficiency, while the implicit one seems to be more robust and accurate. The algorithm validation and its good performance are demonstrated by several two-dimensional examples, including free growth, constrained growth and stress dependent growth.

1. Introduction

Soft materials with a growing mass have drawn wide attentions in recent years, which are complex mechanical materials with typical nonlinear, anisotropic, large strain and inhomogeneous behaviors (Humphrey, 2003; Menzel and Kuhl, 2012).

In the past two decades, continuum theories handling growth phenomena of soft solids within the framework of thermodynamics are well established (Menzel and Kuhl, 2012). The key kinematic assumption is the multiplicative decomposition of deformation gradient tensor into a growth part and an elastic deformation part, which was first adopted in growth mechanics by Rodriguez et al. (1994) to analyze the growth-induced residual stress of biomaterials. The decomposition was originally introduced by Kröner (1959), and then Lee (1969) and Stojanović et al. (1964) made applications to elasto-plastic and thermoelasticity problems at finite strain, respectively. Owing to their work, growth models based on the multiplicative decomposition are predominant in the current literatures for material growth, such as the contributions by Maugin and Imatani (2003), Epstein and Maugin (2000), Kuhl and Steinmann (2003), Lubarda and Hoger (2002), Loret and Simões (2005), Ganghoffer (2013) and Ganghoffer et al. (2014). Other recent developments could be referred to Ciarletta and Maugin (2011) and Ciarletta et al. (2011). In their work, a second gradient theory for material growth and remodeling is developed, which shows that evolution of structural changes is governed by Eshelby-like stress and hyperstress. In addition, another noticeable progress was made by Yavari (2010), in which the growth mechanics was formulated within the context of differential geometry. Ganghoffer and Sokolowski (2014) proposed a micromechanical approach in which the volumetric and surface growth is described in the framework of shape optimization.

Based on the multiplicative decomposition, many theoretical explorations towards engineering applications have been carried out in recent years, such as growth of soft material under geometrical constraint (Ben Amar and Ciarletta, 2010), growing arteries (Goriely and Vandiver, 2010) and growth-induced instabilities and folding in tubular organs (Ben Amar and Goriely, 2005; Ciarletta and Ben Amar, 2012). These works shed light on some basic physical mechanisms of phenomena in growing materials and may provide new methodologies for the studies of growth mechanics. For further background information of growth mechanics, readers are referred to state-of-the-art reviews by Taber (1995), Humphrey (2003), Ambrosi et al. (2011), Cowin (2011) and Jones and Chapman (2012) and the references therein. However, as indicated in the above referred papers, analytical methods

* Corresponding author. Tel./fax: +86 411 84706249.
E-mail address: zhanghw@dlut.edu.cn (H. Zhang).

http://dx.doi.org/10.1016/j.ijsolstr.2014.04.010
0020-7683/

may be helpless to describe the evolution of growth which is very complicated but important to understand it better.

In the numerical aspect, there are also many elaborations based on the multiplicative decomposition. An analogy between the concept of thermal strain in finite deformation and the growth tensor has been made by Feng and coworkers. Based on the idea, they have studied the surface folding of esophageal mucosa (Li et al., 2011a) and surface wrinkling of core–shell structure (Cao et al., 2011; Li et al., 2011b) with the aid of commercial software, Abaqus. Their works make the growth modeling go a big step from labs to engineering applications. However, mass generation or sorption and their influence on material constitutive equations are not fully considered in their model. It seems to be unknown that whether the critical growth factor is in accordance with the theoretical one or not, in spite that good results of buckling mode could be observed in their work. Based on Lubarda and Hoger's work (2002), Himpel et al. (2005) proposed a computational framework to model isotropic multiplicative growth within an implicit nonlinear finite element setting, in which the isotropic stretch ratio is introduced as an internal variable at the integration points. A new incremental tangent modulus is developed in the intermediate or current configuration to reflect the growth influence on the material. Based on the proposed framework, they made several noticeable attempts towards patient specific simulations, such as stress-induced arterial wall growth (Kuhl et al., 2007), cardiac growth, dilation and wall thickening (Göktepe et al., 2010a,b), growing skins beyond the physiological limit (Buganza Tepole et al., 2012) and so on. A summary of their model and related applications could be referred to (Menzel and Kuhl, 2012; Kuhl, 2013). However, the tangent modulus seems to be unsymmetric in some cases (Himpel et al., 2005), which may lead to lower computational efficiency for large scale problems. Meanwhile, the objectivity of tangent modulus is not expounded in detail. In addition, Menzel (2007) developed a remodeling framework for orthotropic continua, in which the reorientation of fiber families in multiplicative anisotropic growth was illuminated. More recently, a stress-induced volumetric material growth model in thermoelastic continua was developed by Vignes and Papadopoulos (2010), where the material growth is regulated by a three-surface activation criterion and corresponding flow rules. There are many other works conducted within the context of mixture theory. For example, Garikepati et al. (2004) proposed a coupling model of mass transport and mechanics, in which the mass change amongst the individual species rather than for a mass exchange with environment was considered. For an improvement version considering the interactions between transport and mechanics is referred to Narayanan et al. (2009). Similarly, Davol et al. (2008) also made many attempts towards a general thermomechanical theory for a mixture of growing elastic constituents with aim to model cartilage growth. Within the framework of the theory of porous media, Ehlers et al. (2009) provided a continuum-biomechanical approach for biological tissue, which extends the classical theory of mixture towards immiscible materials. Though so many attempts have been made for the numerical modeling of growth phenomena, it is still hard to answer which one is the better. Since comparisons of the results with the experiments or analytical solutions are rare, even for the simple case. Actually, many results could only be explained qualitatively in the current stage.

This contribution aims to develop a new computational framework for modeling growth phenomena of soft material following Lubarda and Hoger's work (2002). Unlike the algorithm developed by Himpel et al. (2005) and their follow-up works, which incorporates growth effects into tangent modulus, we introduce the objective Oldroyd stress rate to linearize the nonlinear equation in the current configuration, which is a common practice in nonlinear finite element method (Crisfield, 1997; Wriggers, 2008). Following this line of thought, a new equivalent body force is emerged in the linearized rate equation, which is related to the growth tensor, growth rate, stress, mass generation rate, etc. The force is assured to act as the driver to make the material grow in the numerical aspect. To the authors' knowledge, such kind of numerical implementations for the soft matter with a growing mass have not yet been implemented. The tangent modulus in our model is symmetric, which could be deduced by a subtle change of modulus in the classical FE model without growing mass. The growth tensor and its rate are updated at the Gauss points as internal variables and are used to calculate the growing body force. The final equation is time-dependent and the corresponding integration algorithms are developed. In case the growth rate is dependent on the mechanical quantities or the growth factor itself, an implicit integration scheme is implemented to stabilize the solution.

The paper is organized as follows. In Section 2, the theoretical background for growth mechanics is briefly reviewed and an objective constitutive law is proposed for the linearization of the equation. In Section 3, the finite element implementation and its linearized version are presented in detail. The mechanical variables are updated via a prediction–correction algorithm and the equivalent driving force should be calculated in the prediction step. Both explicit and implicit schemes are explained to integrate the growth tensor. Section 4 presents several numerical examples, including free growth, constrained growth and stress dependent growth, so as to validate the algorithm. Some analytical analyses on the examples and comparison between the implicit and explicit algorithm are also conducted in the section. Finally, conclusions are made in Section 5.

2. Theory

2.1. Kinematics

Consider a continuous elastic body $\mathcal{B}$ described by a set of material points $\mathbf{X}$ in the reference configuration. The motion of body $\mathcal{B}$ is given as a one-parameter family of configuration $\varphi_t : \mathcal{B} \to \mathbb{E}^3$ and the location of point $\mathbf{X}$ at time t becomes

$$\mathbf{x} = \varphi_t(\mathbf{X}) \tag{1}$$

The description of the body at point $\mathbf{x}$ is referred to as the current configuration. Let $\mathbf{F} = \partial\mathbf{x}/\partial\mathbf{X} = \mathrm{Grad}\,\mathbf{x}$ be the deformation gradient tensor, then its multiplicative decomposition, as shown in Fig. 1, is introduced as

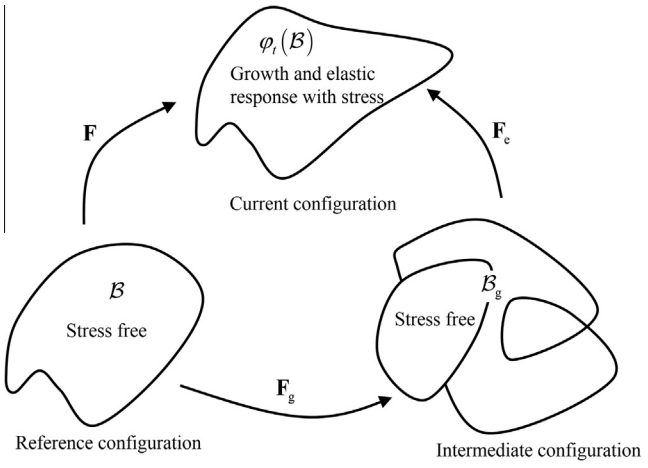

Fig. 1. Decomposition of deformation gradient tensor into a growth part and an elastic part.

$$\mathbf{F} = \mathbf{F}_e \cdot \mathbf{F}_g \tag{2}$$

where $\mathbf{F}_e$ is the elastic deformation tensor describing pure deformation resulting from stress and $\mathbf{F}_g$ is the growth tensor, indicating the generation (or removal) of mass (or volume) at the material point. This decomposition is analogous to the well-known decomposition of elasto-plastic deformation gradient into elastic and plastic parts (Lee, 1969), and was first introduced to the growth of biomaterial by Rodriguez et al. (1994).

Following the basic kinematic assumption, the velocity gradient tensor with respect to the current configuration follows

$$\mathbf{l} = \frac{\partial \mathbf{v}}{\partial \mathbf{x}} = \dot{\mathbf{F}} \cdot \mathbf{F}^{-1} = \dot{\mathbf{F}}_e \cdot \mathbf{F}_e^{-1} + \mathbf{F}_e \cdot \left(\dot{\mathbf{F}}_g \cdot \mathbf{F}_g^{-1}\right) \cdot \mathbf{F}_e^{-1} \tag{3}$$

where $\dot{\mathbf{F}}_e$ and $\dot{\mathbf{F}}_g$ are rate of elastic deformation tensor and growth tensor with respect to the intermediate configuration and the initial configuration, respectively. The initial configuration is coincident with the reference configuration at the beginning of deformation. As a matter of convenience, the symmetric and antisymmetric parts of the terms on the right hand side are introduced as

$$\mathbf{d}_e = \left(\dot{\mathbf{F}}_e \cdot \mathbf{F}_e^{-1}\right)_s, \quad \boldsymbol{\omega}_e = \left(\dot{\mathbf{F}}_e \cdot \mathbf{F}_e^{-1}\right)_a \tag{4}$$

and

$$\mathbf{d}_g = \left[\mathbf{F}_e \cdot \left(\dot{\mathbf{F}}_g \cdot \mathbf{F}_g^{-1}\right) \cdot \mathbf{F}_e^{-1}\right]_s, \quad \boldsymbol{\omega}_g = \left[\mathbf{F}_e \cdot \left(\dot{\mathbf{F}}_g \cdot \mathbf{F}_g^{-1}\right) \cdot \mathbf{F}_e^{-1}\right]_a \tag{5}$$

Therefore, the symmetric and antisymmetric parts of $\mathbf{l}$ could be denoted as

$$\mathbf{d} = \mathbf{d}_e + \mathbf{d}_g, \quad \boldsymbol{\omega} = \boldsymbol{\omega}_e + \boldsymbol{\omega}_g \tag{6}$$

2.2. Equilibrium equations

2.2.1. Continuity equation

As indicated by many authors, growth of soft tissues can be interpreted as a growth of volume with a fixed density (Vignes and Papadopoulos, 2010). Therefore, we assume that the material remains incompressible during mass growth and elastic deformation, i.e.,

$$\rho = \rho_g = \rho_0 \tag{7}$$

Then, we have $J_e = \det \mathbf{F}_e = 1$ and $J = \det \mathbf{F} = J_g = \det \mathbf{F}_g$. It should be noted that the incompressibility assumption is not reasonable for the growth of hard materials, such as bones and horns (Menzel and Kuhl, 2012).

The differential-form continuity equation is (Lubarda and Hoger, 2002)

$$\frac{d}{dt}(\rho J) = r_g J = r_g^0 \tag{8}$$

where d/dt denotes material time derivative and r_g and r_g^0 are the mass growing rate per unit current and initial volume, respectively. For $r_g > 0$, the mass is generated at the material point, and for $r_g < 0$, the mass absorption takes place. There are no volumetric variations in the initial configuration, i.e., $J(\mathbf{X}, 0) = 1$. So integrating Eq. (8) gives

$$\rho J = \rho_0 + \int_0^t r_g^0 d\tau \tag{9}$$

which represents quantity of mass accumulation per initial volume. Due to the incompressibility, Eqs. (8) and (9) could be simplified as

$$\rho_0 \dot{J}_g = \rho_0 \dot{J} = r_g^0 \tag{10}$$

and

$$J = J_g = 1 + \frac{1}{\rho_0} \int_0^t r_g^0 d\tau \tag{11}$$

Using the relation $J_g = \det \mathbf{F}_g$ and the definition $\rho_g^0 = \rho_0 J_g$, Eq. (10) could be expressed as

$$\rho_g^0 \mathrm{tr}\left(\dot{\mathbf{F}}_g \cdot \mathbf{F}_g^{-1}\right) = r_g^0 \tag{12}$$

which indicates that the mass source r_g^0 is dependent on growth tensor and its rate. We should note that if r_g^0 is given as a specified field instead of $\mathbf{F}_g$ or $\dot{\mathbf{F}}_g$, additional equations should be supplied to determine $\dot{\mathbf{F}}_g$. In the paper, we consider the former case and thus r_g^0 does not enter into the final equation.

2.2.2. Balance of momentum

Neglecting the inertial effects and the diffusion force arising from interaction between different constituents (Cowin and Hegedus, 1976; Klisch et al., 2001), the equilibrium equation in a growing body is the same as that in traditional cases (Lubarda and Hoger, 2002), which read

$$\nabla \cdot \boldsymbol{\sigma} + \mathbf{b} = \mathbf{0} \tag{13}$$

and

$$\boldsymbol{\sigma} = \boldsymbol{\sigma}^{\mathrm{T}} \tag{14}$$

Here, $\boldsymbol{\sigma}$ is Cauchy stress and $\mathbf{b}$ is the volumetric force per current volume.

2.3. Constitutive equations

2.3.1. Constitutive equations for mechanical field

Due to the assumption of incompressibility in Eq. (7), the strain energy function per unit volume in the intermediate configuration could be written as (Lubarda and Hoger, 2002; Ben Amar and Goriely, 2005; Menzel, 2007; Ciarletta and Maugin, 2011)

$$W_g = J_g W_0 \tag{15}$$

where W_0 is the strain energy function per unit volume without mass growth. If mass increases at a material point, then $J_g > 1$ and $W_g > W_0$, which means that the strain energy after growth is greater than that without growth for the same strain state. On the contrary, in case $J_g < 1$, mass absorption leads to a reduction of strain energy. The second Piola–Kirchhoff stress defined in the initial configuration could be denoted by

$$\mathbf{S} = \frac{\partial W_g}{\partial \mathbf{E}} = \frac{\partial W_g}{\partial \mathbf{E}_e} : \frac{\partial \mathbf{E}_e}{\partial \mathbf{E}} = \mathbf{F}_g^{-1} \cdot \frac{\partial W_g}{\partial \mathbf{E}_e} \cdot \mathbf{F}_g^{-\mathrm{T}} = \mathbf{F}_g^{-1} \cdot \mathbf{S}_e \cdot \mathbf{F}_g^{-\mathrm{T}} \tag{16}$$

which could be considered as the stress tensor pulled back from configuration $\mathcal{B}_g$ to $\mathcal{B}$. Here, $\mathbf{E} = \frac{1}{2}\left(\mathbf{F}^{\mathrm{T}} \cdot \mathbf{F} - \mathbf{I}\right)$, $\mathbf{E}_e = \frac{1}{2}\left(\mathbf{F}_e^{\mathrm{T}} \cdot \mathbf{F}_e - \mathbf{I}\right) = \frac{1}{2}(\mathbf{C}_e - \mathbf{I})$, and $\mathbf{S}_e$ is the stress tensor defined in the intermediate configuration $\mathcal{B}_g$. The Kirchhoff stress could be introduced by a push-forward of $\mathbf{S}$,

$$\boldsymbol{\tau} = \mathbf{F} \cdot \mathbf{S} \cdot \mathbf{F}^{\mathrm{T}} = \mathbf{F}_e \cdot \mathbf{S}_e \cdot \mathbf{F}_e^{\mathrm{T}} \tag{17}$$

To linearize the nonlinear equation, the change rate of $\boldsymbol{\tau}$ should be deduced. Here, the method in Lubarda and Hoger (2002) is inherited, but distinctions could also be detected comparing with traditional numerical methods, such as the implementation in Himpel et al. (2005). Differentiating $\boldsymbol{\tau}$ with respect to time yields

$$\dot{\boldsymbol{\tau}} = \left(\dot{\mathbf{F}}_e \cdot \mathbf{F}_e^{-1}\right) \cdot \boldsymbol{\tau} + \boldsymbol{\tau} \cdot \left(\dot{\mathbf{F}}_e \cdot \mathbf{F}_e^{-1}\right)^{\mathrm{T}} + \mathbf{F}_e \cdot \left(\mathbf{C} : \dot{\mathbf{E}}_e\right) \cdot \mathbf{F}_e^{\mathrm{T}} + \frac{\partial \boldsymbol{\tau}}{\partial J_g} \frac{r_g^0}{\rho_0} \tag{18}$$

where $\mathbf{C}$ is constitutive tensor defined on $\mathcal{B}$ with the form

$$\mathbf{C} = \frac{\partial \mathbf{S}_e}{\partial \mathbf{E}_e} = \frac{\partial^2 W_g}{\partial \mathbf{E}_e \otimes \partial \mathbf{E}_e} \tag{19}$$

It should be noticed that $\dot{\boldsymbol{\tau}}$ does not satisfy objectivity, which is an inevitable prerequisite for the formulation of constitutive equations. Therefore, the objective Lie derivative of $\boldsymbol{\tau}$ is introduced as

$$\dot{\boldsymbol{\tau}}_{\mathrm{T}} = \dot{\boldsymbol{\tau}} - \mathbf{l}\cdot\boldsymbol{\tau} - \boldsymbol{\tau}\cdot\mathbf{l}^{\mathrm{T}} \tag{20}$$

Here, $\dot{\boldsymbol{\tau}}_{\mathrm{T}}$ is also called as the Oldroyd stress rate or the Truesdell rate of Kirchhoff stress. Combining Eqs. (6), (18), and (20), we have

$$\dot{\boldsymbol{\tau}}_{\mathrm{T}} = \mathbf{c}:\mathbf{d} - \mathbf{c}:\mathbf{d}_{\mathrm{g}} - (\mathbf{d}_{\mathrm{g}}+\boldsymbol{\omega}_{\mathrm{g}})\cdot\boldsymbol{\tau} - \boldsymbol{\tau}\cdot(\mathbf{d}_{\mathrm{g}}-\boldsymbol{\omega}_{\mathrm{g}}) + \frac{\partial\boldsymbol{\tau}}{\partial J_{\mathrm{g}}}\frac{r_{\mathrm{g}}^{0}}{\rho_{0}} \tag{21}$$

where $\mathbf{c}$ is a fourth-order constitutive tensor in the current configuration and could be deduced by a push-forward operation on $\mathbf{C}$

$$c_{ijkl} = F^{\mathrm{e}}_{ip}F^{\mathrm{e}}_{jq}F^{\mathrm{e}}_{kr}F^{\mathrm{e}}_{ls}C_{pqrs} \tag{22}$$

In general, the elastic deformation tensor, $\mathbf{F}_{\mathrm{e}}$, is not dependent on J_{g} directly, therefore,

$$\frac{\partial\boldsymbol{\tau}}{\partial J_{\mathrm{g}}} = \frac{\partial}{\partial J_{\mathrm{g}}}\left(\mathbf{F}_{\mathrm{e}}\cdot\mathbf{S}_{\mathrm{e}}\cdot\mathbf{F}_{\mathrm{e}}^{\mathrm{T}}\right) = \mathbf{F}_{\mathrm{e}}\cdot\mathbf{S}_{e0}\cdot\mathbf{F}_{\mathrm{e}}^{\mathrm{T}} = \boldsymbol{\tau}_{0} \tag{23}$$

where $\mathbf{S}_{e0} = \frac{\partial W_0}{\partial \mathbf{E}_{\mathrm{e}}}$. Eqs. (18)–(21) could be used to linearize the nonlinear FE equation and the tangent modulus $\mathbf{c}$ is symmetric which follows almost the same calculating procedure as that in the cases without mass growth (Wriggers, 2008). The growth effects are reflected in the last four terms of Eq. (21), which lead to an equivalent growth-driving body force in the final equation, see Section 3.

2.3.2. Constitutive equation for growth field

The rigorous approach to appropriately characterize the evolution of growth tensor uniformly is still lacking and remains a challenging task in current growth theories, since growth phenomena are related to many sophisticated phenomena, such as gene expression, concentration of each constituent and material microstructure. Generally, individual growth law should be specified with respect to different tissues (Kuhl, 2013). Even so, many attempts on the evolution equation of growth have been made, such as a stress-driven equation by Göktepe et al. (2010a), strain-driven area growth of skin by Buganza Tepole et al. (2012), a multiphase model considering the effect of fluid and fiber-reinforced solid by Grillo et al. (2012) and a general form based on the dissipation inequality for open system by Menzel and Kuhl (2012). Following their ideas, we adopt a general evolution form

$$\dot{\mathbf{F}}_{\mathrm{g}} = \mathbf{f}(\mathbf{F}_{\mathrm{g}}, \mathbf{M}) \tag{24}$$

where $\mathbf{M}$ denotes some kinds of mechanical quantities, such as stress or strain in either intermediate or current configuration. The specific growth laws are different for each kind of growth and illustrated with numerical examples in Section 4.

3. Numerics

3.1. Weak form of equilibrium and its linearization

The weak form of equilibrium equation (13) with respect to the current configuration $\varphi(\mathcal{B})$ has the following form

$$\mathcal{G}(\boldsymbol{\varphi}, \mathbf{u}_{\mathrm{v}}) = \int_{\varphi(\mathcal{B})}\boldsymbol{\sigma}:\frac{\partial\mathbf{u}_{\mathrm{v}}}{\partial\mathbf{x}}dv - \int_{\varphi(\mathcal{B})}\mathbf{b}\cdot\mathbf{u}_{\mathrm{v}}dv - \int_{\varphi(\partial\mathcal{B}_{\sigma})}\mathbf{t}\cdot\mathbf{u}_{\mathrm{v}}da \tag{25}$$

where $\mathbf{u}_{\mathrm{v}}$ is the virtual velocity, $\mathbf{b}$ is the body force per current volumetric, dv, and $\mathbf{t}$ is the surface traction. The Cauchy stress, $\boldsymbol{\sigma}$, is related to $\mathbf{t}$ by $\mathbf{t} = \mathbf{n}\cdot\boldsymbol{\sigma}$, where $\mathbf{n}$ is the unit outward normal to the surface of current configuration. Let the virtual velocity gradient be

$$\mathbf{l}_{\mathrm{v}} = \frac{\partial\mathbf{u}_{\mathrm{v}}}{\partial\mathbf{x}} \tag{26}$$

Its symmetric part is denoted as $\mathbf{d}_{\mathrm{v}} = \frac{1}{2}\left(\mathbf{l}_{\mathrm{v}} + \mathbf{l}_{\mathrm{v}}^{\mathrm{T}}\right)$. Therefore, internal virtual work could be reformulated as

$$\mathcal{G}_{\mathrm{int}}(\boldsymbol{\varphi}, \mathbf{u}_{\mathrm{v}}) = \int_{\varphi(\mathcal{B})}\boldsymbol{\sigma}:\mathbf{l}_{\mathrm{v}}dv = \int_{\mathcal{B}}\boldsymbol{\tau}:\mathbf{l}_{\mathrm{v}}dV \tag{27}$$

in which, $\boldsymbol{\tau} = J\boldsymbol{\sigma}$ and $dv = JdV$. Linearization of above equation leads to

$$\mathcal{G}_{\mathrm{int}}(\boldsymbol{\varphi}, \mathbf{u}_{\mathrm{v}})\cdot\dot{\mathbf{u}} = \int_{\mathcal{B}}(\dot{\boldsymbol{\tau}}:\mathbf{l}_{\mathrm{v}} + \boldsymbol{\tau}:\dot{\mathbf{l}}_{\mathrm{v}})dV \tag{28}$$

where $\dot{\mathbf{u}}$ is the change rate of displacement. Using Eqs. (20) and (21), and $\dot{\mathbf{l}}_{\mathrm{v}} = -\mathbf{l}_{\mathrm{v}}\cdot\mathbf{l}$, the internal virtual work has the form

$$\mathcal{G}_{\mathrm{int}}(\boldsymbol{\varphi}, \mathbf{u}_{\mathrm{v}})\cdot\dot{\mathbf{u}} = \int_{\mathcal{B}}\left(\mathbf{d}_{\mathrm{v}}:\mathbf{c}:\mathbf{d} + \boldsymbol{\tau}:\left(\mathbf{l}_{\mathrm{v}}^{\mathrm{T}}\cdot\mathbf{l}\right) + \mathbf{d}_{\mathrm{v}}:\dot{\boldsymbol{\tau}}_{\mathrm{g}}\right)dV \tag{29}$$

where

$$\dot{\boldsymbol{\tau}}_{\mathrm{g}} = -\mathbf{c}:\mathbf{d}_{\mathrm{g}} - (\mathbf{d}_{\mathrm{g}}+\boldsymbol{\omega}_{\mathrm{g}})\cdot\boldsymbol{\tau} - \boldsymbol{\tau}\cdot(\mathbf{d}_{\mathrm{g}}-\boldsymbol{\omega}_{\mathrm{g}}) + \frac{r_{\mathrm{g}}^{0}}{\rho_{0}}\boldsymbol{\tau}_{0} \tag{30}$$

We could find that $\dot{\boldsymbol{\tau}}_{\mathrm{g}}$ is related to variables in the current configuration, including tangent modulus, growth tensor, elastic deformation tensor, growth rate, stress state and mass source. If no growth is introduced to the material, i.e., $\dot{\mathbf{F}}_{\mathrm{g}} = 0$, then $\dot{\boldsymbol{\tau}}_{\mathrm{g}}$ would vanish due to Eqs. (5) and (12). Therefore, $\dot{\boldsymbol{\tau}}_{\mathrm{g}}$ should be an integrated quantity, which is conjugated to the velocity gradient and reflects the effects of mass growth on the linearized virtual work. For some further details about linearization backgrounds, readers are referred to the monograph by Crisfield (1997) or Wriggers (2008).

3.2. Finite element discretization

To construct the discretized equation, the domain, $\mathcal{B}$, is partitioned into n_e finite elements

$$\mathcal{B} = \bigcup_{e=1}^{n_e}\mathcal{B}_e \tag{31}$$

Here, n_e is the number of elements. Interpolations of the mechanical field on an element, $\mathcal{B}_e$, could be expressed as

$$\mathbf{u}_{\mathrm{v}}^{\mathrm{h}} = \sum_{i=1}^{n_d}\mathbf{N}_i\mathbf{p}_{vi}, \quad \dot{\mathbf{u}}^{\mathrm{h}} = \sum_{i=1}^{n_d}\mathbf{N}_i\dot{\mathbf{p}}_i \tag{32}$$

where $\mathbf{p}_i$ ($\mathbf{p}_{vi}$) is the (virtual) node displacement, $\mathbf{N}_i$ is the corresponding base function and n_d is the node number of the element. The vector form of virtual velocity gradient and its symmetric part could be expressed as

$$\mathbf{l}_{\mathrm{v}}^{\mathrm{h}} = \sum_{i=1}^{n_d}\mathbf{G}_i\mathbf{p}_{\mathrm{v}i}, \quad \mathbf{d}_{\mathrm{v}}^{\mathrm{h}} = \sum_{i=1}^{n_d}\mathbf{B}_i\dot{\mathbf{p}}_{\mathrm{v}i} \tag{33}$$

where $\mathbf{G}_i$ and $\mathbf{B}_i$ are the derivative matrix of the base function corresponding to node i. Using Eqs. (25), (29), and (33), the discretized increment equation follows

$$(\mathbf{K}_{\mathrm{m}} + \mathbf{K}_{\sigma})\dot{\mathbf{p}} = \dot{\mathbf{f}}_{\mathrm{g}} + \dot{\mathbf{f}}_{\mathrm{ext}} \tag{34}$$

where $\mathbf{K}_{\mathrm{m}}$ and $\mathbf{K}_{\sigma}$ are material and geometrical stiffness matrix with the following forms

$$\mathbf{K}_{\mathrm{m}} = \sum_{e=1}^{n_e}\int_{\mathcal{B}_e}\mathbf{B}^{\mathrm{T}}\mathbf{D}\mathbf{B}dV, \quad \mathbf{K}_{\sigma} = \sum_{e=1}^{n_e}\int_{\mathcal{B}_e}\mathbf{G}^{\mathrm{T}}\hat{\boldsymbol{\tau}}\mathbf{G}dV \tag{35}$$

and $\dot{\mathbf{f}}_{\mathrm{g}}$ is the change rate of equivalent body force with the form

$$\dot{\mathbf{f}}_{\mathrm{g}} = -\sum_{e=1}^{n_e}\int_{\mathcal{B}_e}\mathbf{B}^{\mathrm{T}}\dot{\boldsymbol{\tau}}_{\mathrm{g}}dV \tag{36}$$

In Eq. (35), $\hat{\boldsymbol{\tau}} = \mathrm{diag}(\overline{\boldsymbol{\tau}}, \overline{\boldsymbol{\tau}})$ and $\overline{\boldsymbol{\tau}} = \begin{bmatrix} \tau_{11} & \tau_{12} \\ \tau_{21} & \tau_{22} \end{bmatrix}$ for two-dimensional cases and readers could find $\hat{\tau}$ for other cases in Crisfield (1997). The stiffness in Eq. (35) is almost the same as that of the classical Updated Lagrangian (U.L.) scheme. For the details, see the monograph by Crisfield (1997) or Wriggers (2008). It also needs to be noted that the constitutive modulus and Kirchhoff stress are revised by the growth term, since the modification of strain energy function due to growth is considered, see Eq. (15). The constitutive matrix $\mathbf{D}$ is composed by the component of $\mathbf{c}$ in Eq. (22) and its numerical implementations for two-dimensional plane stress cases could be referred to Gruttmann and Taylor (1992) and Reese and Wriggers (1995).

From Eqs. (30) and (36), we could find that $\dot{\mathbf{f}}_{\mathrm{g}}$ is related to constitutive modulus, stress state, growth tensor, elastic deformation and mass generation rate in the current configuration. If no growth appears in the material, i.e., $\dot{\boldsymbol{\tau}}_{\mathrm{g}} = \mathbf{0}$, then $\dot{\mathbf{f}}_{\mathrm{g}}$ would become zero. That is to say, $\dot{\mathbf{f}}_{\mathrm{g}}$ does not arise in the linearized equation of classical problems without mass growth. Actually, $\dot{\mathbf{f}}_{\mathrm{g}}$ could be considered as a state-dependent body force rate, which integrates the effects of several factors, such as the configuration, stress, growth speed and so on. Therefore, $\dot{\mathbf{f}}_{\mathrm{g}}$ should be the driver which forces the material to grow in the numerical aspect. To the authors' knowledge, this concept is first proposed in computational growth mechanics.

Assuming that there is no residual stress in the initial configuration, that is, $\boldsymbol{\tau} = \boldsymbol{\tau}^0 = \mathbf{0}$ and in this condition, $\mathbf{K}_\sigma = \mathbf{0}$, then, Eq. (34) degenerates to

$$\mathbf{K}_{\mathrm{m}}^0 \dot{\mathbf{p}}^0 = \dot{\mathbf{f}}_{\mathrm{g}}^0 + \dot{\mathbf{f}}_{\mathrm{ext}}^0 \tag{37}$$

where the subscript '0' denotes the quantity with respect to the initial configuration and the rate of growth body force follows

$$\dot{\mathbf{f}}_{\mathrm{g}}^0 = -\sum_{e=1}^{n_e} \int_{\mathcal{B}_e} \mathbf{B}^{\mathrm{T}} \dot{\boldsymbol{\tau}}_{\mathrm{g}}^0 dV \tag{38}$$

Here, $\dot{\boldsymbol{\tau}}_{\mathrm{g}}^0 = -\mathbf{c} : \mathbf{d}_{\mathrm{g}}^0$. We could easily figure out that Eq. (37) is similar to that of thermal stress analysis at small strain and $\mathbf{d}_{\mathrm{g}}^0$ could be analogous to initial thermal strain for small deformation in a way. Actually, Yavari (2010) has pointed out that "the growth result in eigenstrain is very similar to those of classical linear thermoelasticity" and a comparison study of constitutive theories based on multiplicative decomposition by Lubarda (2004) has also drawn similar conclusions.

3.3. Integration algorithm

The linearized equation (34) in the configuration $\varphi_t(\mathcal{B})$ is assumed to be

$$\left(\mathbf{K}_{\mathrm{m}}^t + \mathbf{K}_\sigma^t\right)\dot{\mathbf{p}}^t = \dot{\mathbf{f}}_{\mathrm{g}}^t + \dot{\mathbf{f}}_{\mathrm{ext}}^t \tag{39}$$

Solving the deformation rate, $\dot{\mathbf{p}}^t$, the displacement at time $t + \Delta t$ is updated by

$$\mathbf{p}^{t+\Delta t} = \mathbf{p}^t + \dot{\mathbf{p}}^t \Delta t \tag{40}$$

Then, the mechanical fields at $t + \Delta t$, such as stress and constitutive modulus, could be calculated directly using $\mathbf{p}^{t+\Delta t}$. It is not hard to understand that the numerical solution should approximate to the true solution for a small enough Δt. However, for some complicated growth modes, Eq. (40) may induce errors for the unknowns, $\mathbf{p}^{t+\Delta t}$, if Δt is not so small enough. Therefore, some corrections on the prediction results $\mathbf{p}^{t+\Delta t}$ are needed to stabilize the solution. Here is the equation at the correction step n

$$\left(\mathbf{K}_{\mathrm{m},n}^t + \mathbf{K}_{\sigma,n}^t\right)\Delta \mathbf{p}_n^t = \mathbf{f}_{\mathrm{ext}}^{t+\Delta t} - \mathbf{f}_{\mathrm{int},n}^t \tag{41}$$

where subscript n denotes the correction step and the internal force $\mathbf{f}_{\mathrm{int}} = \sum_{e=1}^{n_e} \int_{B_e} \mathbf{B}^{\mathrm{T}} \boldsymbol{\tau} dV$. The displacement after n corrections could be expressed as

$$\mathbf{p}_n^{t+\Delta t} = \mathbf{p}_{n-1}^{t+\Delta t} + \Delta \mathbf{p}_n^t \tag{42}$$

At the first correction step, $\mathbf{p}_0^{t+\Delta t}$ is equal to $\mathbf{p}^{t+\Delta t}$ in Eq. (40). The correction iterations would be terminated in case

$$\|\Delta \mathbf{p}_n^t\| / \|\mathbf{p}_n^{t+\Delta t}\| < \varepsilon_p \tag{43}$$

where ε_p is a prescribed convergence tolerance. Actually, the above correction process is very similar to that of classical Newton–Raphson iteration (Wriggers, 2008).

Integration of growth tensor is carried on in the level of Gauss integration points. Here, we adopt the explicit forward Euler method

$$\mathbf{F}_{\mathrm{g}}^{t+\Delta t} = \mathbf{F}_{\mathrm{g}}^t + \dot{\mathbf{F}}_{\mathrm{g}}^t \Delta t \tag{44}$$

where the growth rate, $\dot{\mathbf{F}}_{\mathrm{g}}^t$, could be calculated directly by Eq. (24). However, the explicit algorithm may induce numerical instability even for a lightly large time increment Δt, so we develop a more stable implicit algorithm to update the growth tensor

$$\mathbf{F}_{\mathrm{g}}^{t+\Delta t} = \mathbf{F}_{\mathrm{g}}^t + \left(\kappa \dot{\mathbf{F}}_{\mathrm{g}}^t + (1-\kappa)\dot{\mathbf{F}}_{\mathrm{g}}^{t+\Delta t}\right)\Delta t \tag{45}$$

where κ is a parameter in the range $0 \leqslant \kappa \leqslant 1$ and determines the precision of integration. In case $\mathbf{F}_{\mathrm{g}}^{t+\Delta t}$ is only dependent on $\mathbf{F}_{\mathrm{g}}^{t+\Delta t}$ rather than the mechanical quantities $\mathbf{M}^{t+\Delta t}$ ($\mathbf{M}^{t+\Delta t}$ could denote either stress or strain), Eq. (45) is just a traditional nonlinear equation which can be solved by the classical Newton–Raphson algorithm. A similar implicit algorithm, based on a residual equation similar to Eq. (44), has been developed by Buganza Tepole et al. (2012) and Göktepe et al. (2010a). However, the case will be more complicated supposing that $\dot{\mathbf{F}}_{\mathrm{g}}^{t+\Delta t}$ relies on both $\mathbf{F}_{\mathrm{g}}^{t+\Delta t}$ and $\mathbf{M}_{\mathrm{g}}^{t+\Delta t}$ at $t + \Delta t$, which are both unknown in advance. In this case, an improved iterative scheme is employed

$$\mathbf{F}_{\mathrm{g},m}^{t+\Delta t} = \mathbf{F}_{\mathrm{g}}^t + \left(\kappa \dot{\mathbf{F}}_{\mathrm{g}}^t + (1-\kappa)\dot{\mathbf{F}}_{\mathrm{g},m-1}^{t+\Delta t}\right)\Delta t \tag{46}$$

where $\mathbf{F}_{\mathrm{g},m}^{t+\Delta t}$ is the growth tensor at the iteration step m and

$$\dot{\mathbf{F}}_{\mathrm{g},m-1}^{t+\Delta t} = \mathbf{f}\left(\mathbf{F}_{\mathrm{g},m-1}^{t+\Delta t}, \mathbf{M}_{m-1}^{t+\Delta t}\right) \tag{47}$$

The iterative process is terminated under the conditions

$$\left\|\mathbf{F}_{\mathrm{g},m}^{t+\Delta t} - \mathbf{F}_{\mathrm{g},m-1}^{t+\Delta t}\right\| \Big/ \left\|\mathbf{F}_{\mathrm{g},m-1}^{t+\Delta t}\right\| < \varepsilon_F \text{ or } m > m_{\mathrm{crit}} \tag{48}$$

where ε_F and m_{crit} are the convergence tolerance and the critical iteration step. For the first step, the explicit updating Eq. (44) is adopted and the iteration enters into the second step unconditionally. We should note that, in each iteration step, a full mechanical analysis should be conducted, that is, Eqs. (39)–(42), to obtain the mechanical quantity $\mathbf{M}_{m-1}^{t+\Delta t}$. For growth modes with a constant rate, i.e., $\dot{\mathbf{F}}_{\mathrm{g}}^t = \dot{\mathbf{F}}_{\mathrm{g}}^{t+\Delta t} = const$, or a special coefficient $\kappa = 1$, Eq. (43) degenerates to the forward Euler integration equation, $\mathbf{F}_{\mathrm{g}}^{t+\Delta t} = \mathbf{F}_{\mathrm{g}}^t + \dot{\mathbf{F}}_{\mathrm{g}}^t \Delta t$.

3.4. Flowchart

To elaborate the algorithm more clearly, its flowchart is shown in Fig. 2. There are two main parts in the whole flow: mechanical analysis in the global level and growth tensor updating in the Gauss integration points level. In the mechanical analysis part, the prediction step and correction iterative steps are included. The equivalent body force, driving the material to grow, is calculated in the prediction step, which shows distinctions with the traditional methods. Both explicit and implicit schemes are employed to integrate the growth tensor.

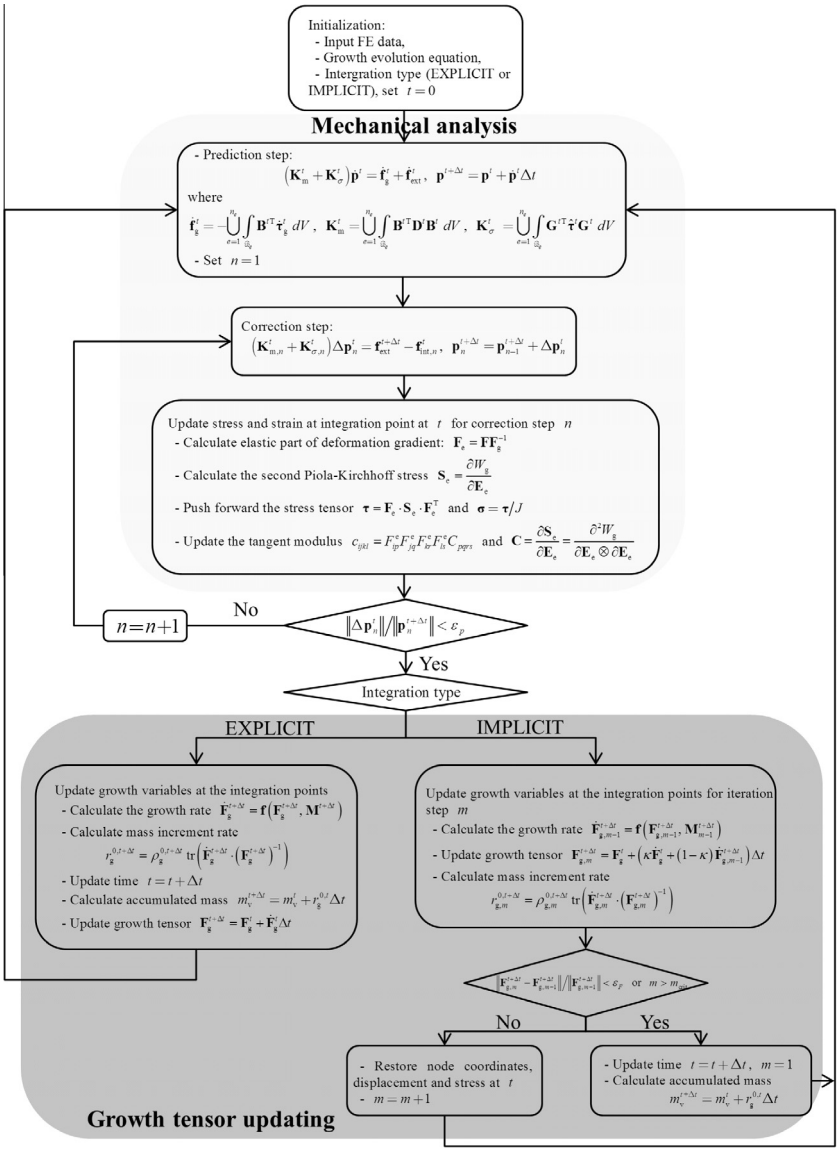

Fig. 2. Flowchart of the algorithm.

4. Numerical examples

In this section, some typical growth phenomena in nature and engineering are investigated qualitatively or quantitatively, which involve free growth, constrained growth and stress dependent growth. The first two types of growth modes are relatively simple, and thus we adopt the explicit algorithm to update growth tensor. The evolution of growth tensor in the last example is more complicated and both implicit and explicit algorithms are implemented and compared with each other. The final time is set to one if the growth mode is time-independent. In the current studies, all examples are simplified as two-dimensional plane stress cases and the incompressible condition $J_{\mathrm{e}}=1$ could be satisfied precisely by eliminating the deformation out of plane in the strain energy function (Crisfield, 1997).

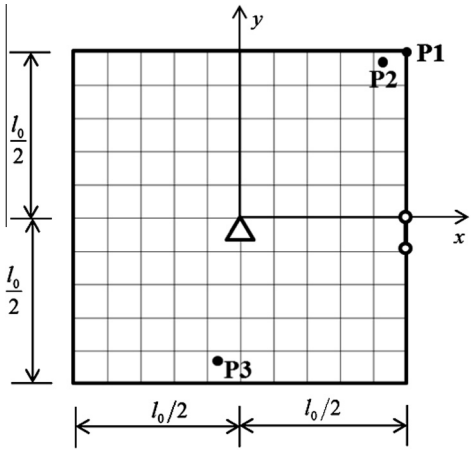

Fig. 3. Free growth model.

4.1. Free growth

Free growth refers to the growth with no constraints. Free growth phenomena are widely observed in nature, such as the surface buckling of pumpkins (Yin et al., 2009) and leaves (Liang and Mahadevan, 2009), where the growth-induced deformation leads to self-equilibrium residual stress, which promotes the morphological change. The mechanisms of some engineering applications,

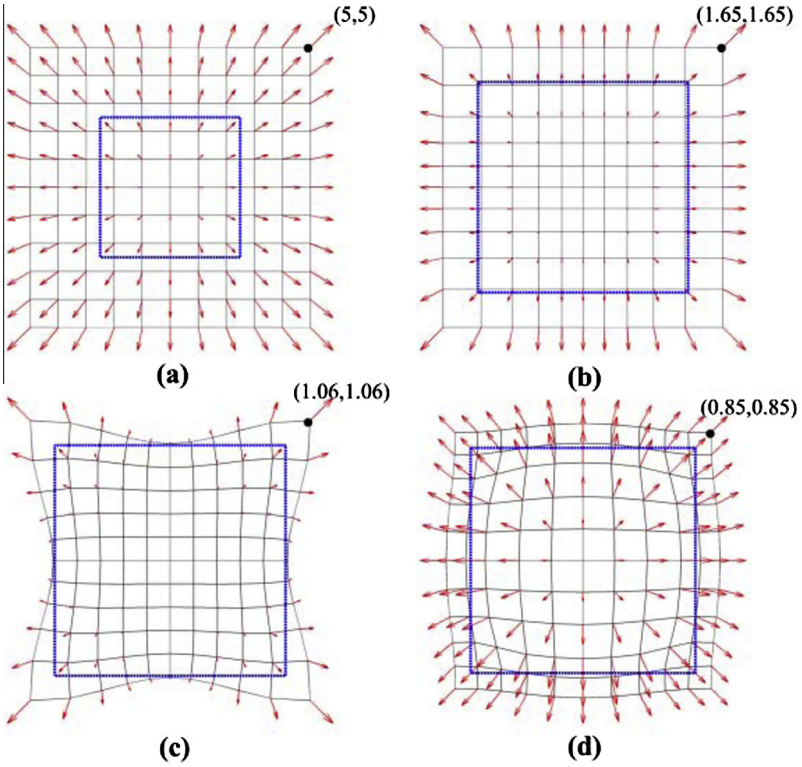

Fig. 4. (a)–(d) show the configuration before and after growth for growth modes M1–M4, respectively. The direction and size of displacements are denoted by red arrows. The values of the points marked by solid dots are given as the reference value. The blue rectangular is the initial configuration. (For interpretation of the references to colour in this figure legend, the reader is referred to the web version of this article.)

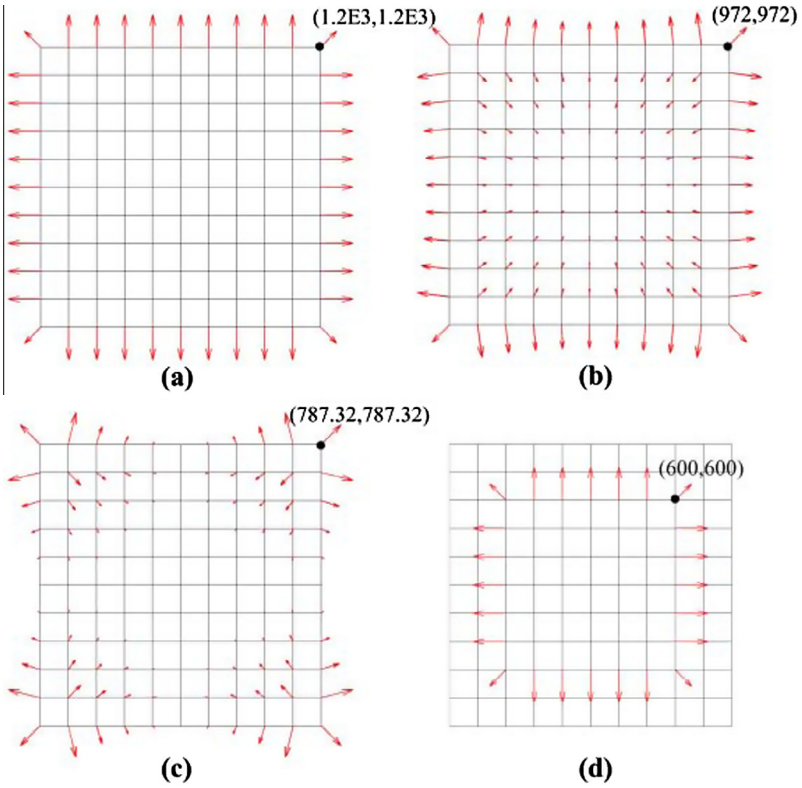

Fig. 5. The driving body force of growth at the first step, (a)–(d) correspond to the growth modes M1–M4, respectively. The direction and size of forces are denoted by red arrows. The values of the points marked by solid dots are given as the reference value. (For interpretation of the references to colour in this figure legend, the reader is referred to the web version of this article.)

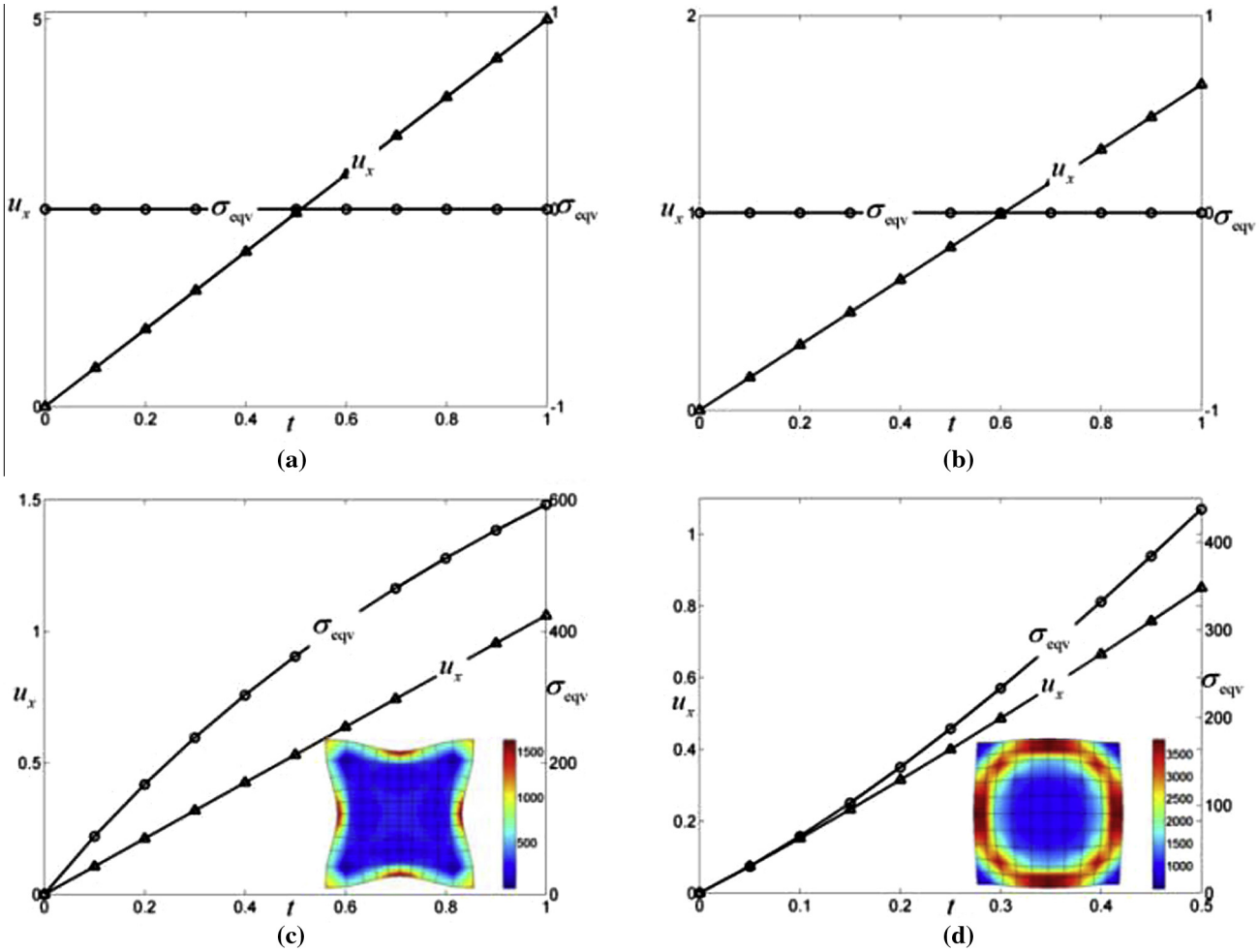

Fig. 6. Evolution of displacement at point P1 and Von Mises stress at point P2 with respect to growth factor, points P1 and P2 are marked in Fig. 3. (a)–(d) Correspond to growth modes M1–M4, respectively. The subgraph in (c) and (d) are the final distribution of Von Mises stress.

such as swelling a gel (Kim et al., 2012) and dehydration of beans (Li et al., 2011b), are also similar to free growth. For a theoretical investigation about this topic, see Yavari (2013) and the related references therein. Here, we adopt a simple concept in Zimmerman et al. (2009), which aims to calculate an atomic-scale deformation gradient with atomistic simulation. Supposing that the growth displacement is continuous and the elastic deformations are assumed to vanish, then no residual stress will be induced and the intermediate configuration becomes the current one. In such case,

$$\mathbf{F}_g = \frac{\partial \mathbf{x}}{\partial \mathbf{X}} \tag{49}$$

and it could be proved that

$$\mathbf{F}_g \times \nabla = \mathbf{0} \text{ or } \frac{\partial F^g_{ik}}{\partial x_m}\varepsilon_{kmj} = 0 \tag{50}$$

where ε_{kmj} is the permutation tensor defined as

$$\varepsilon_{kmj} = \begin{cases} 1 & \text{when } k,m,j \text{ are } 1,2,3 \text{ or an even permutation of } 1,2,3, \\ -1 & \text{when } k,m,j \text{ are an odd permutation of } 1,2,3, \text{ e.g., } 2,1,3, \\ 0 & \text{when any two indices are equal} \end{cases} \tag{51}$$

Ignoring the rotation part of $\mathbf{F}_g$, then $\mathbf{F}_g = \mathrm{diag}(\vartheta_x, \vartheta_y, \vartheta_z)$ and Eq. (50) becomes

$$\begin{bmatrix} 0 & -\frac{\partial \vartheta_x}{\partial z} & \frac{\partial \vartheta_x}{\partial y} \\ \frac{\partial \vartheta_y}{\partial z} & 0 & -\frac{\partial \vartheta_y}{\partial x} \\ -\frac{\partial \vartheta_z}{\partial x} & \frac{\partial \vartheta_z}{\partial y} & 0 \end{bmatrix} = \mathbf{0} \tag{52}$$

The above equation yields,

$$\vartheta_x = \vartheta_x(x), \quad \vartheta_y = \vartheta_y(y), \quad \vartheta_z = \vartheta_z(z) \tag{53}$$

which indicates that if the growth stretch in a direction depends on the coordinates in the same direction, no residual stress will be induced by free growth. It also should be noted that ϑ_x, ϑ_y and ϑ_z should satisfy C_0 continuity across the domain and discontinuity points will also induce residual stress, see the details in the follow-up examples.

4.1.1. Free growth with a constant rate

Based on the above theoretical background, the free growth of a two-dimensional square block with the edge length $l_0 = 10$ is introduced, in which only the rigid displacement is constrained as shown in Fig. 3. The domain is discretized by 10×10 Q4 elements. Incompressible Neo-Hookean material is adopted with a strain energy function

$$W_g = J_g C_0 \left(\alpha_x^2 + \alpha_y^2 + \alpha_z^2 - 3\right) \tag{54}$$

where $J_g = \det \mathbf{F}_g$ (see Eq. (15) for its meaning) and $C_0 = 2000$ is the shear modulus at the ground state, α_x, α_y and α_z are three main

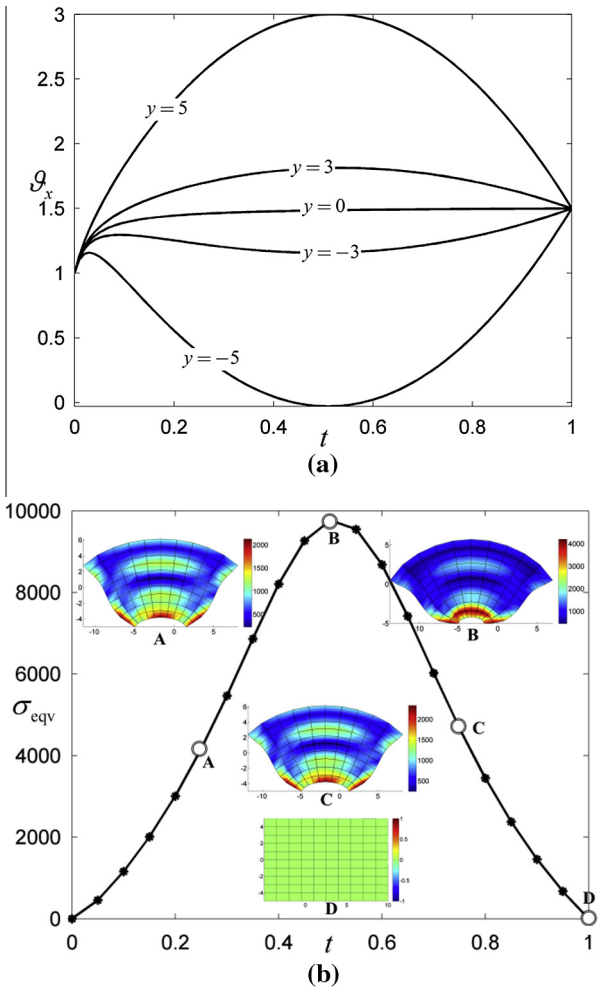

Fig. 7. (a) Evolution of growth factor ϑ_x with respect to t at different positions, (b) Von Mises stress at point P3 in Fig. 3 and their distributions on the deformed configuration at several steps.

stretches elastic deformation gradient $\mathbf{F}_e$, which satisfy $\alpha_x\alpha_y\alpha_z = 1$ due to the incompressibility.

For this example, we choose four growth modes as follows to verify the algorithm: M1: constant growth, $\vartheta_x = \vartheta_y = 2$; M2: position dependent growth with quadratic distribution, $\vartheta_x = 1 + \frac{x^2}{25}$, $\vartheta_y = 1 + \frac{y^2}{25}$; M3: position dependent growth with biquadratic distribution, $\vartheta_x = \vartheta_y = 1 + \frac{x^2y^2}{625}$; M4: self-constrained growth, $\vartheta_x = \vartheta_y = \begin{cases} 1.5, & \text{when } -3 \leqslant x \leqslant 3,\ -3 \leqslant y \leqslant 3 \\ 1, & \text{otherwise} \end{cases}$. The first three modes are continuous and the final one is not.

The results for growth modes M1–M4 are shown in Figs. 4–6. The final deformations for four growth modes are depicted in Fig. 4, in which the blue line denotes the initial configuration of the block. The corresponding equivalent driving body force (rate) for the first step, which is shown in Eq. (38) and decided by the distribution of $\mathbf{d}_g^0 = \dot{\mathbf{F}}_g^0$ (since $\mathbf{F}_g^0 = \mathbf{F}_e^0 = \mathbf{I}$ in the initial configuration), is shown in Fig. 5. In Fig. 6, evolution of displacement and Von Mises stress at the points P1 and P2, marked in Fig. 3, with respect to growth factor are given.

For constant growth M1, the growth expansion at each point is the same and the domain expands uniformly as is expected, see Fig. 4(a). The driving body force, shown Fig. 5(a), is distributed uniformly along the boundary of the square and vanishes within the domain, which is very similar to a negative hydrostatic pressure. As pointed out in Section 3.2, $\mathbf{d}_g^0$ could be analogous to initial thermal strain for small deformation in a way, so readers could understand the distribution of equivalent body force by analogy to that of thermal stress analysis. For quadratic growth, M2, a non-uniform deformation, which is large in the areas close to the boundary and small in the center, is induced as shown in Fig. 4(b). The corresponding driving force (in Fig. 5(b)) is distributed outward on the boundary and inward inside the domain. Therefore, the deformation grows larger near the domain boundary. From Fig. 6(a) and (b), we can find that Von Mises stress for both modes M1 and M2 remains zero with respect to different growth quantities. The reason lies in that the growth factor in a direction is dependent on the coordinates in the same direction for M1 and M2, which shows accordance with the analytical results in Eq. (53). It is interesting that the non-uniform deformation for M2 does not lead to residual stress. It should be mentioned that no correction steps or equilibrium iterations are needed in these two cases; that is to say, the equivalent body force drives the body to equilibrium configuration directly, which convinces us of the function of the driving force.

For growth mode M3, more complicated deformation and body force appear as shown in Figs. 4(c) and 5(c). We could note that deformations at $x = 0$ and $y = 0$ are zero and at the four corners become large, which is in accordance with the growth mode. The deformation of self-constrained growth, M4, and the corresponding driving force are shown in Figs. 4(d) and 5(d). As we can see, self-constraint induced by exterior materials imposes a restriction on the inner material with constant growth and leads to a complex non-uniform deformation. The displacement and Von Mises stress curves for M3 and M4 are shown in Fig. 6(c) and (d), which all appear as nonlinear relations. The largest stress for M3 comes up at the middle point of each edge, where strong compression occurs due to the growth of surrounding material. For the self-constrained growth, strong compression also occurs due to the constraint of exterior materials and thus large stress appears close to the interfaces of growing and non-growing areas.

4.1.2. Free growth with a time dependent growth rate

The work of Ehlers et al. (2009) gives the evolution of a free swelling gel which shows large similarities with an existing experiment. Their simulation is implemented on the FE package PANDAS

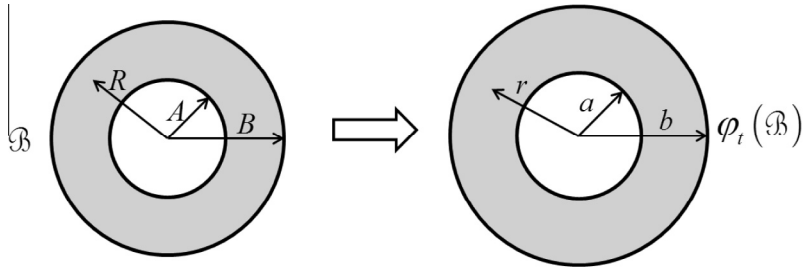

Fig. 8. Configurations of the circular ring before and after symmetric growth.

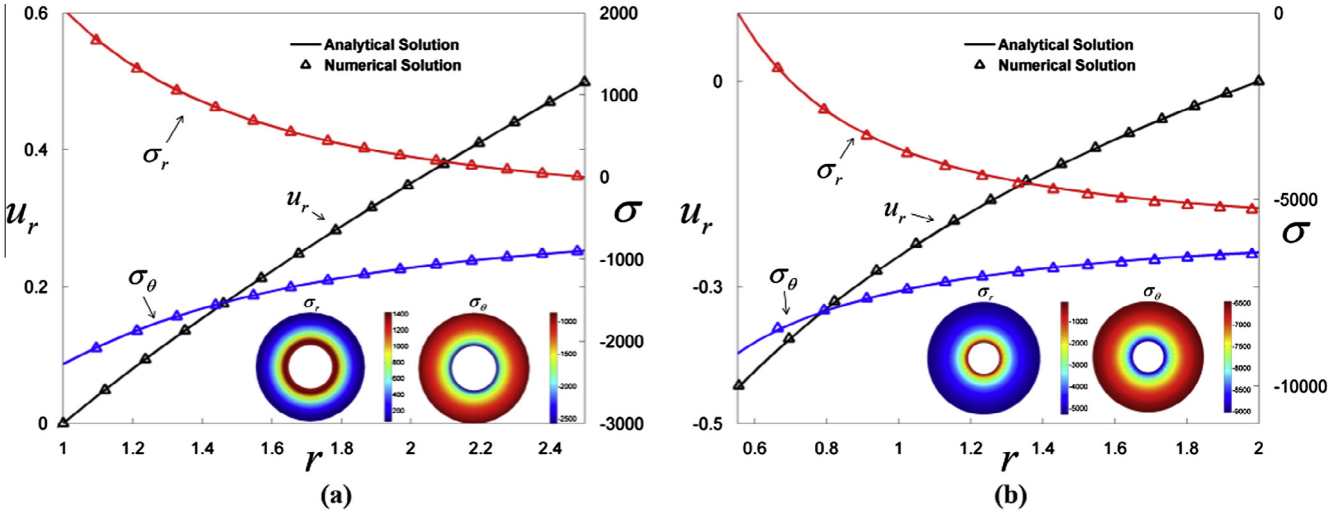

Fig. 9. Displacement and stress results of transversally isotropic growth, M1, with (a) inner and (b) external constraints.

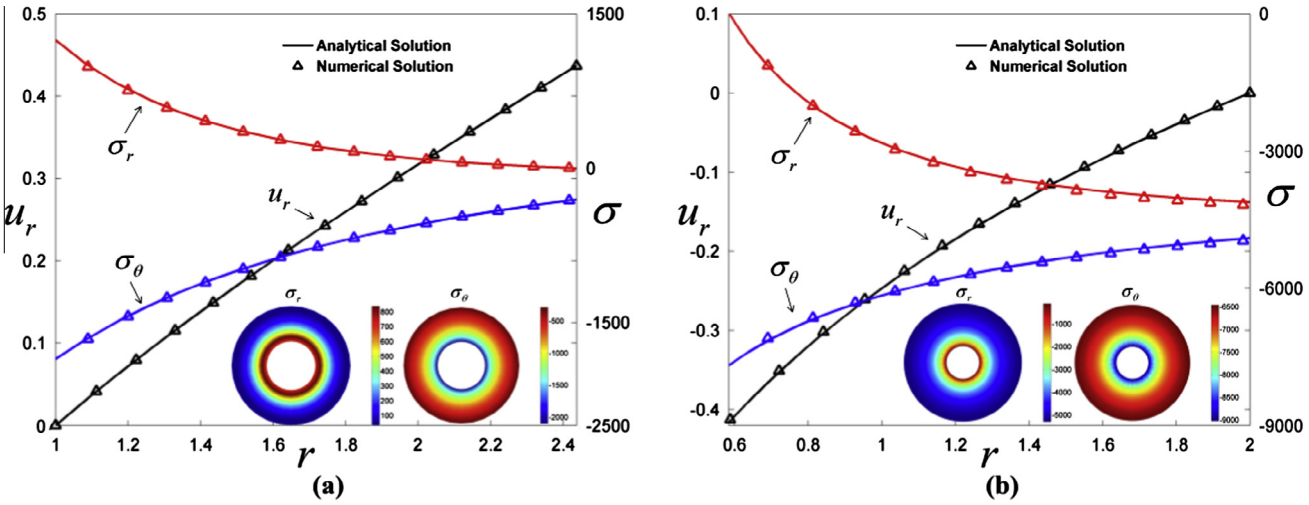

Fig. 10. Displacement and stress results of anisotropic growth, M2, with (a) inner and (b) external constraints.

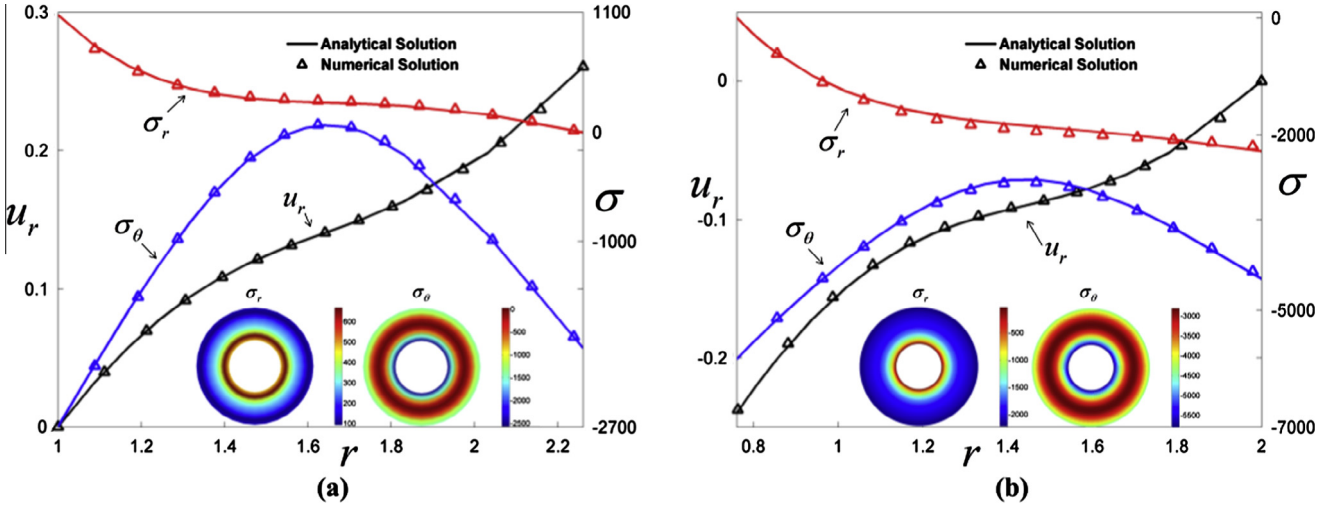

Fig. 11. Displacement and stress results of isotropic position dependent growth, M3, with (a) inner and (b) external constraints.

within the framework of the theory of porous media. The swelling media is treated as biphasic, four-component aggregate, where fluid transport, ion diffusion and electrical potential of electrostatic are considered, and the swelling deformation is induced by chemical diffusion. Here, we adopt a similar example with theirs in our developed numerical scheme with aim to reproduce their results. It should be noted that our model is based on the continuum growth theory of homogenous media and the morphological transformation is realized by the evolution of the growth tensor. For simplicity, the model is inherited from last example without changing the geometric and material parameters and the rigid displacement is constrained by a simply-supported boundary condition at $(-5,-5)$ and $(5,-5)$, see Fig. 3. The evolution of growth factor in the range $0 \leqslant t \leqslant 1$ is assumed to be

$$\vartheta_x = \left(\frac{1}{-60t - 1.9374} + 0.5161\right)\left[\frac{y^3}{10}\left(-t^2 + t\right) + 1\right] + 1, \quad \vartheta_y = 1 \tag{55}$$

where ϑ_x depends on both position and time, which is close to 1 at $t = 0$ and equals to 1.5 at $t = 1$.

Changes of ϑ_x with y equal to -5, -3, 0, 3, 5 are depicted in Fig. 7(a), which indicates that the upper material ($y > 0$) always expands and the lower material ($y < 0$) mainly appears shrinkage. Both the expansion and the shrinkage reach the maximum at about $t = 0.5$. Under such growing mode, we could obtain Von Mises Stress at Gauss Point P3 marked in Fig. 3 with respect to time, as shown in Fig. 7(b), which increases at the initial time steps and then decreases to zeros at the last step. Von Mises stress distributions on several deformed configurations at the steps A–D are also shown in Fig. 7(b). At step B, both deformation and stress reach the maximum, since growth between the areas of $y > 0$ and $y < 0$ shows the largest discrepancies. Comparing the results with the first example in Ehlers et al. (2009), a great similarly could be found in both deformation and stress. We should note that quantitative comparison with that in Ehlers et al. (2009) is a little hard since the evolution law of growth factor should be constructed based on experiments.

4.2. Constrained growth of a circular ring

Constraints could also induce stress in a growing matter, even if Eq. (53) is satisfied. Here, we consider the symmetric growth of a circular ring with a variable thickness as shown in Fig. 8. The position of material points at R in the reference configuration becomes r in the current configuration after growth. The material behavior is assumed to be Neo-Hookean, as shown in Eq. (54). The growth mode could be denoted as $\mathbf{F}_g = \mathrm{diag}(\vartheta_r, \vartheta_\theta, 1)$ in cylindrical coordinates, where ϑ_r and ϑ_θ are growth factors in the radial and circumferential directions. Due to symmetry, ϑ_r and ϑ_θ are only related to R.

The plane strain case with a constant thickness has been investigated comprehensively by Dervaux and Ben Amar (2011) and Li et al. (2011a), with applications to buckling condensation of a ring and surface folding of esophageal mucosa, respectively. It seems that material growth in plane stress case with variable thickness remains unsolved. Therefore, we first conduct some analytical analyses about the growth ring, see the details in the Appendix. Though the final results are semi-analytical, but it could be used to validate our algorithm.

For this example, we consider three kinds of growth modes: M1: transversely isotropic growth, $\vartheta_r = \vartheta_\theta = 1.35$; M2: anisotropic growth, $\vartheta_r = 1.35$, $\vartheta_\theta = 1.25$; M3: position dependent growth, $\vartheta_r = \vartheta_\theta = (R - 1.5)^2 + 1.1$, and two kinds of boundary conditions: B1: inner constraint, $u_r(a) = 0$, $\sigma_r(b) = 0$; B2: external constraint, $u_r(b) = 0$, $\sigma_r(a) = 0$. Therefore, there are six cases by combining three growth modes and two boundary conditions.

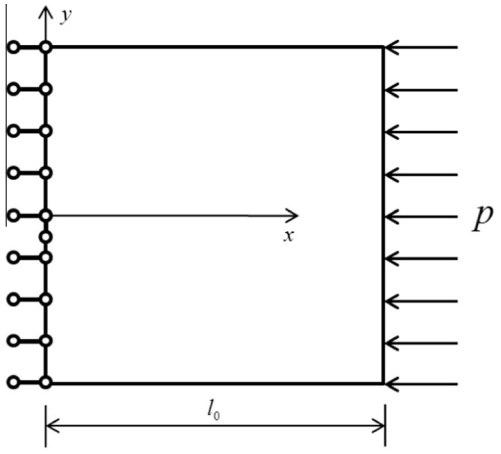

Fig. 12. Growth model of the bone block.

Table 1
The parameters for the stress-dependent-growth block in Fig. 12.

l_0	b_0	C_0	N	k_y	σ_x^*	ρ_0	Δt
10	1	50	−100	0.5	−4.5	1	0.03

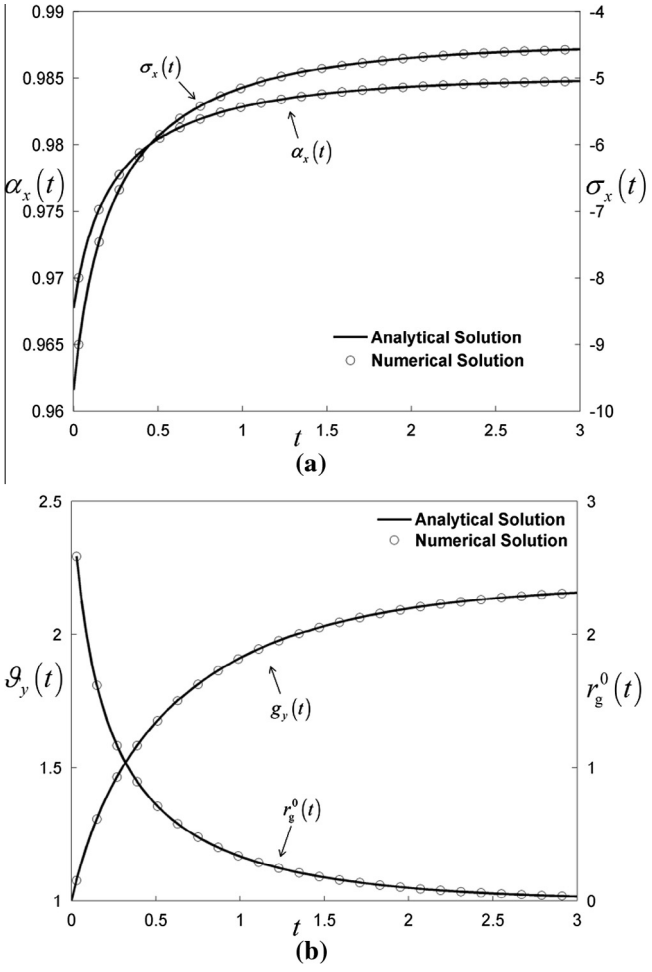

Fig. 13. Evolution of results with respect to time for the growth bone block model in Fig. 12, (a) shows elastic deformation α_x and Cauchy stress σ_x, and (b) shows growth factor ϑ_y and mass source rate r_g^0.

In the initial configuration, the inner radius A and outer radius B are set to 1 and 2, respectively. The modulus of Neo-Hookean material C_0 is 2000 and the domain is discretized by 14×80 Q8 elements in the radial and circumferential directions. The analytical and numerical results, depicted in Figs. 9–11, agree well for all cases, which indicate the effectiveness of the model.

The radial stress is positive in the inner constrained case and decreases to zero at the outer radius (see Figs. 9(a), 10(a) and 11(a)); while the outer radius is constrained, the radius stress becomes negative and vanishes at the inner radius (see Figs. 9(b), 10(b) and 11(b)). For all cases, circumferential pressure is observed due to the constraints, which is larger at the inner radius for all growth modes. An extreme point for circumferential pressure appears for M3, which shows distinct difference with the monotonic trends of M1 and M2, since the growth factor at the middle point of radius is the smallest.

4.3. Stress dependent growth

4.3.1. Stress dependent growth of a square block

It has been realized that growth alters the stress distribution and stress modulates growth in return. Here, we take an example transformed from Goriely et al. (2008), where growth is a function of stress tensor. As shown in Fig. 12, a bone block is applied with a uniform pressure $p = N/A$, where N is a constant resultant force, $A = bl$ is the area of loading surface in the current configuration, l and b are the length and thickness of the block. As the stress in the x direction, σ_x, exceeds an critical value σ_x^*, the domain begins to grow in the y direction. Then, it reduces σ_x and the growth rate also decreases. This reduces σ_x in turn until σ_x reaches the critical value. The growth mode is homogenous and no additional constraints are applied, so no residual stress will arise. The material of the block is assumed to be incompressible Neo-Hookean material with stain energy function as Eq. (54), and the elastic deformation tensor could be denoted as

$$\mathbf{F}_e = \mathrm{diag}\left(\alpha_x, \frac{1}{\sqrt{\alpha_x}}, \frac{1}{\sqrt{\alpha_x}}\right) \tag{56}$$

The only non-vanishing Cauchy stress in the x direction is

$$\sigma_x = 2C_0\left(\alpha_x^2 - \frac{1}{\alpha_x}\right) \tag{57}$$

If σ_x after the initial equilibrium is greater than σ_x^*, the body begins to grow in the y direction as the following rate

$$\dot{\vartheta}_y(t) = \begin{cases} k_y(|\sigma_x(t)| - |\sigma_x^*|), & \text{if } |\sigma_x(t)| > |\sigma_x^*|, \\ 0, & \text{else} \end{cases} \tag{58}$$

where k_y is the coefficient adjusting the growth rate. The block growth only happens in the y direction, so the deformation gradient tensor could be denoted by

$$\mathbf{F} = \mathrm{diag}\left(\alpha_x, \frac{\vartheta_y}{\sqrt{\alpha_x}}, \frac{1}{\sqrt{\alpha_x}}\right) \tag{59}$$

The area of loading surface after deformation is $A = l_0 b_0 \vartheta_y / \alpha_x$. Using equilibrium equation $\sigma_x A = N$, we could get the following equation about α_x,

$$\alpha_x^3 - \frac{N}{2C_0 l_0 b_0 \vartheta_y}\alpha_x^2 - 1 = 0 \tag{60}$$

Eqs. (58) and (60) are strongly coupled and could be solved by the forward Euler method

$$\vartheta_y(t + \Delta t) = \vartheta_y(t) + \dot{\vartheta}_y(t)\Delta t \tag{61}$$

The initial value of the above integration $\vartheta_y(0)$ is 1. Finally, substituting $\vartheta_y(t + \Delta t)$ into Eq. (60), α_x could be solved numerically.

The typical geometric and material parameters are listed in Table 1. The time increment, Δt, is set to 0.03 and there are totally 100 incremental steps with a total time $t = 3$. The domain is discretized by 10×10 Q4 elements. The semi-analytical and numerical results are depicted in Fig. 13 in absolute value, which shows the evolutions of α_x and σ_x in (a) and ϑ_y and r_g^0 in (b). As we can see, all the numerical results agree well with the semi-analytical one, which indicates the accuracy of the developed numerical method.

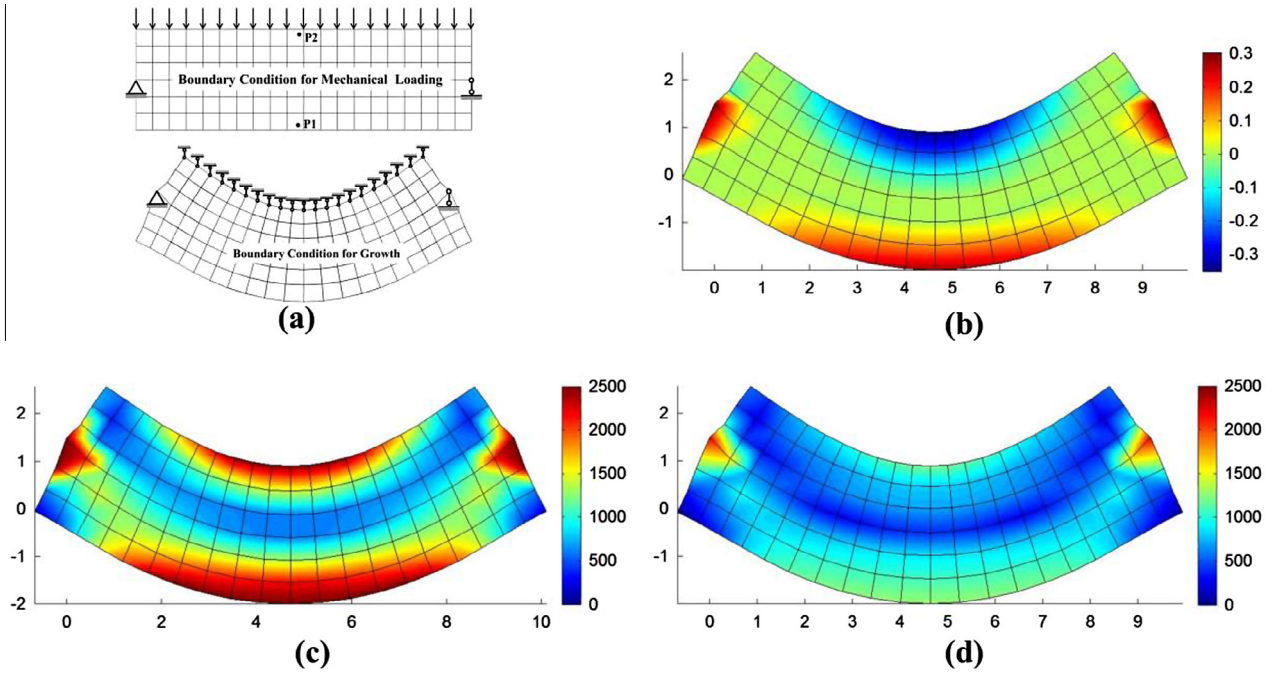

Fig. 14. (a) Shows the boundary conditions for mechanical loading and growth, (b) shows mass change at $t = 1$, (c) and (d) are the Von Mises stress at $t = 0$ and $t = 1$.

From a physical standpoint, all quantities changes dramatically at the initial steps and tend to be stable at the final steps. At the initial equilibrium, r_g^0 is equal to -9.68, which is greater than the critical value -4.5, then the domain begins to grow in the y direction. The growth leads to the decline of σ_x, which results in the reduction of $\dot{\vartheta}_y(t)$ and r_g^0 in return, and finally the overall system tends towards stability. The pressure stress and corresponding deformation decrease with time, which indicates the self-adaptive ability of biological material in response to the external stimuli.

4.3.2. Stress dependent growth of a beam

Living matter can autonomously respond to environment and can develop and adapt itself in respond to external stimuli. Here, we further discuss this topic in the developed algorithm within explicit and implicit integration schemes. The simply supported rectangular beam, with an initial size $a_0 \times b_0$, is applied with a uniform vertical force p on each node of the top surface at the initial time. Then, the vertical displacement on the top surface are constrained after equilibrium, as shown in Fig. 14(a), and the body begins to grow as the following evolution equation (Lubarda and Hoger, 2002; Göktepe et al., 2010a; Buganza Tepole et al., 2012)

$$\dot{\vartheta}_x = \dot{\vartheta}_y = \dot{\vartheta}_g = k_g(\vartheta_g)\phi_g(\boldsymbol{\sigma}) \tag{62}$$

where the limiting growth function $k_g(\vartheta_g)$ and growth criterion $\phi_g(\boldsymbol{\sigma})$ satisfy, respectively,

$$k_g(\vartheta_g) = \frac{1}{\tau}\left(\frac{\vartheta_{max} - \vartheta_g}{\vartheta_{max} - 1}\right)^{\gamma} \tag{63}$$

and

$$\phi_g(\boldsymbol{\sigma}) = \begin{cases} (|\mathrm{tr}(\boldsymbol{\sigma})| - \sigma_{crit})\mathrm{sign}(\mathrm{tr}(\boldsymbol{\sigma})), & \text{if } |\mathrm{tr}(\boldsymbol{\sigma})| > \sigma_{crit} \\ 0, & \text{else} \end{cases} \tag{64}$$

Here, $1/\tau$ and γ modulate the growth speed and the nonlinearity of growth process (Göktepe et al., 2010a), σ_{crit} is a positive critical stress limit which activates the growth process, tr(•) and sign(•) are the trace of a tensor and the sign of a number. We could find that if $\mathrm{tr}(\boldsymbol{\sigma}) > \sigma_{crit}$, then $\phi_g(\boldsymbol{\sigma}) > 0$, which indicates mass increase; if $\mathrm{tr}(\boldsymbol{\sigma}) < -\sigma_{crit}$, then $\phi_g(\boldsymbol{\sigma}) < 0$ and mass absorption happens. It should be noted that Göktepe et al. (2010a) have suggested that ϕ_g should be expressed in terms of elastic part of deformation gradient $\mathbf{F}_e$ or the so-called Mandel stress $\mathbf{M}_e = \mathbf{C}_e \cdot \mathbf{S}_e$. Here, the adopted Cauchy stress $\boldsymbol{\sigma}$ should not change the fundamental properties of the problem and provides convenience for results discussion.

The body is composed by Neo-Hookean material with strain energy function shown in Eq. (54). The domain is meshed with 6×20 Q4 elements. The related geometric and material parameters are listed in Table 2. For this example, we choose three time increments, $\Delta t = 0.01, 0.04, 0.07$, for both explicit and implicit integration schemes. In the implicit algorithm, the coefficient κ in Eq. (45) is set to be 0.75. The evolution of Von Mises stress at points P1 and P2, marked in Fig. 14(a), are depicted in Figs. 15(a) and (b), respectively. As we can see, the curves with respect $\Delta t = 0.01$ for both schemes are almost the same, so the results in this case could be considered as the reference solution. As $\Delta t = 0.04$, the result of explicit algorithm shows larger deviation with the reference solution than that of the implicit algorithm. Especially, large oscillations could be observed in Fig. 15(b) for the curve of explicit algorithm. Even so, Von Mises stress seems to converge to the correct one for both integration schemes in this case. However, time increment 0.07 will make the result of explicit algorithm divergent (not shown in the figure), while that for implicit scheme remains the tendency to the exact solution at the last several steps yet. So it can be concluded that the implicit scheme shows more robustness and higher precision than the explicit integration scheme. We should also mention that more computation is demanded for implicit scheme.

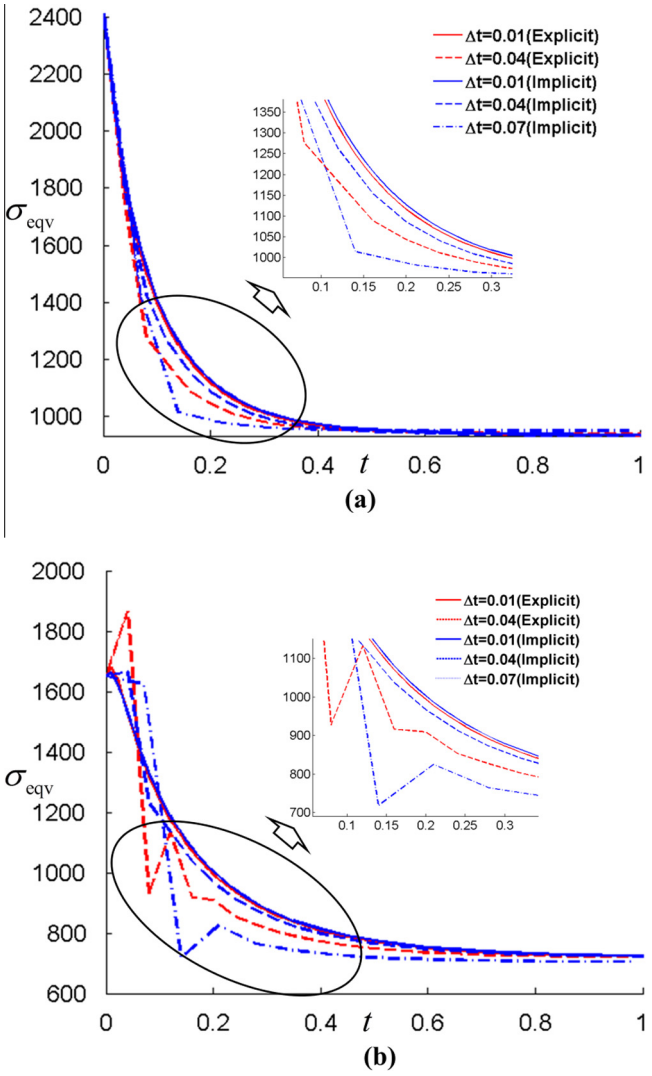

Fig. 15. (a) And (b) are the evolution of Von Mises stress at the points P1 and P2 marked in Fig. 14(a). The results with respect to the time increments Δt = 0.01, 0.04, 0.07 for both explicit and implicit schemes are shown.

Comparing Fig. 14(c) with Fig. 14(d), Von Mises stress decreases remarkably from the beginning to the end of growth. The areas with Von Mises stress greater than 2500, such as the bottom and top surfaces, almost disappear. So growth gives rise to the decrease of Von Mises stress, which indicates the effects of the growth law, i.e., Eq. (62), and the stress modulation on growth. From Fig. 14(b), which gives the distribution of mass generation per unit volume, given in Eq. (9), we could find that mass is generated mainly nearby the bottom surface and disappears on the top surface. The phenomenon is not hard to be understood, since the top and bottom materials are in the states of compression and tension, which lead to $\mathrm{tr}(\boldsymbol{\sigma}) < 0$ and $\mathrm{tr}(\boldsymbol{\sigma}) > 0$, respectively.

Table 2
The parameters for the stress-dependent-growth beam shown in Fig. 14(a).

a_0	b_0	C_0	p	$1/\tau$	γ	σ_{crit}	ρ_0
10	3	2000	−150	0.001	2	1000	1

5. Conclusions

A new nonlinear FE algorithm for modeling deformation and stress of soft materials with a growing mass is developed. We develop a new linearization scheme for the nonlinear equation based on the objective Oldroyd stress rate. Within this scheme, an equivalent body force, derived from growth tensor, its rate, etc. is detected, which seems to be the driving force to make the material grow in the numerical aspect. Both explicit and implicit integration schemes are developed to solve the time-related equation. Several kinds of numerical examples, such as free growth, constrained growth and stress dependent growth, are introduced, which show the robustness and accuracy of the algorithm. The constrained growth in Section 4.2 indicates that the FE algorithm is capable to capture the complicated distribution of residual stress precisely. The last stress-dependent-growth example demonstrates the higher robustness and accuracy of the implicit integration scheme, which shows the applicability of the algorithm in realistic problems with complicated growth law and boundary conditions. The FE equations are constructed in the current configuration based on the updated Lagrangian formulation, which provides more convenience to consider the fluid–solid interactions and the relevant boundary conditions (Narayanan et al., 2009).

The algorithm is also promising to be provided as a tool for modeling deformation induced by illumination, dehydration, PH and so on. For example, specified nonuniform growth patterns could induce different buckled surfaces of a thermal responsive gel plate, which shows great potential for design of complex actuating structures (Kim et al., 2012). Another example is the non-Euclidean plate with a non-zero Gaussian curvature, which could be generated by natural growth or different swelling (Efrati et al., 2009). The corresponding numerical method for modeling such phenomena seems to be rare for predicting complex patterns. Such phenomena show similar characters with the mass growth and should follow the same numerical scheme. This topic is waited for future investigations. In our algorithm, the introduced examples are not specific biological tissues or organs; to monitor the behavior of true biological materials, with more complicated constitutive law, geometries and loading conditions, will be the future work.

Acknowledgements

The supports of the National Natural Science Foundation (11232003, 91315302, 11072051), the Ph.D. Programs Foundation of Ministry of Education (20130041110050), the 111 Project (B08014) and the National Key Basic Research Special Foundation of China (2010CB832704) are gratefully acknowledged.

Appendix A. Symmetric growth of a ring with a variable thickness

For the symmetric growth of a ring, deformation gradient could be defined as

$$\mathbf{F} = \mathrm{diag}(r', r/R, \lambda_t) \tag{A.1}$$

where $r' = \partial r/\partial R$ and λ_t denotes the deformation gradient in the thickness direction. We first consider a constant growth tensor, $\mathbf{F}_g = \mathrm{diag}(\vartheta_r, \vartheta_\theta, 1)$, where ϑ_r and ϑ_θ are constant growth factor in the radial and circumferential directions. Therefore, the elastic deformation can be denoted as

$$\mathbf{F}_e = \mathbf{F}\cdot\mathbf{F}_g^{-1} = \mathrm{diag}\left(\frac{1}{\vartheta_r}r', \frac{1}{\vartheta_\theta}\frac{r}{R}, \lambda_t\right) = \mathrm{diag}(\alpha_r, \alpha_\theta, \alpha_z) \tag{A.2}$$

The strain energy for incompressible Neo-Hookean material is

$$W = J_g C_0(\alpha_r^2 + \alpha_\theta^2 + \alpha_z^2 - 3) \tag{A.3}$$

where $J = \det\mathbf{F} = \det\mathbf{F}_g = \vartheta_r\vartheta_\theta$ and $\alpha_r\alpha_\theta\alpha_z = 1$ due to the incompressibility. So the Cauchy stress follows

$$\sigma_r = 2C_0(\alpha_r^2 - \alpha_r^{-2}\alpha_\theta^{-2}), \quad \sigma_\theta = 2C_0(\alpha_\theta^2 - \alpha_r^{-2}\alpha_\theta^{-2}) \tag{A.4}$$

The equilibrium equation in the current configuration has the form

$$\frac{d\sigma_r}{dr} + \frac{1}{r}(\sigma_r - \sigma_\theta) = 0 \tag{A.5}$$

Substituting Eq. (A.4) into Eq. (A.5), the following nonlinear equation about r could be obtained

$$2\vartheta_\theta^2 r + 2\vartheta_r^4\vartheta_\theta^4\left(R^2 r^{-2} r'^{-4} r + R^2 r^{-3} r'^{-2} - R r^{-2} r'^{-3}\right) + \vartheta_\theta^2 r^{-1} r'^2 - \vartheta_r^2 r/R^2 = 0 \tag{A.6}$$

It can be easily seen that Eq. (A.6) is a second-order differential equation with high nonlinearity. In case ϑ_r and ϑ_θ are position dependent, the corresponding equation will be more complicated. It seems to be impossible to solve it analytically and here, we ask for the help of numerical method. For the constrained symmetric growth, the symmetric Diriclet and Neumann boundary conditions are

$$u_r|_{r=r_0} = \overline{u}_r \tag{A.7}$$

and

$$\sigma_r|_{r=r_0} = \overline{\sigma}_r \tag{A.8}$$

where $\overline{u}_r$ and $\overline{\sigma}_r$ are the known displacements and stress at $r = r_0$. After obtaining r and r', the stress could be calculated by Eq. (A.4).

References

Ambrosi, D., Ateshian, G.A., Arruda, E.M., Cowin, S.C., Dumais, J., Goriely, A., Holzapfel, G.A., Humphrey, J.D., Kemkemer, R., Kuhl, E., Olberding, J.E., Taber, L.A., Garikipati, K., 2011. Perspectives on biological growth and remodeling. J. Mech. Phys. Solids 59 (4), 863–883.

Ben Amar, M., Ciarletta, P., 2010. Swelling instability of surface-attached gels as a model of soft tissue growth under geometric constraints. J. Mech. Phys. Solids 58 (7), 935–954.

Ben Amar, M., Goriely, A., 2005. Growth and instability in elastic tissues. J. Mech. Phys. Solids 53 (10), 2284–2319.

Buganza Tepole, A., Gosain, A.K., Kuhl, E., 2012. Stretching skin: the physiological limit and beyond. Int. J. Nonlinear Mech. 47 (8), 938–949.

Cao, Y.P., Li, B., Feng, X.Q., 2011. Surface wrinkling and folding of core–shell soft cylinders. Soft Matter 8 (2), 556–562.

Ciarletta, P., Ben, Amar M., 2012. Growth instabilities and folding in tubular organs: a variational method in non-linear elasticity. Int. J. Nonlinear Mech. 47 (2), 248–257.

Ciarletta, P., Maugin, G.A., 2011. Elements of a finite strain-gradient thermo-mechanical theory for material growth and remodeling. Int. J. Nonlinear Mech. 46 (10), 1341–1346.

Ciarletta, P., Ambrosi, D., Maugin, G.A., 2011. Mass transport in morphogenetic processes: a second gradient theory for volumetric growth and material remodeling. J. Mech. Phys. Solids 60 (3), 432–450.

Cowin, S.C., 2011. The specific growth rates of tissues: a review and a re-evaluation. J. Biomech. Eng. 133 (4), 041001.

Cowin, S.C., Hegedus, D.H., 1976. Bone remodeling I: theory of adaptive elasticity. J. Elast. 6 (3), 313–326.

Crisfield, M.A., 1997. Non-linear Finite Element Analysis of Solids and Structure, vol. 2. John Wiley, Chichester, UK.

Davol, A., Bingham, M.S., Sah, R.L., Klisch, S.M., 2008. A nonlinear finite element model of cartilage growth. Biomech. Model. Mechanobiol. 7 (4), 295–307.

Dervaux, J., Ben, Amar M., 2011. Buckling condensation in constrained growth. J. Mech. Phys. Solids 59 (3), 538–560.

Efrati, E., Sharon, E., Kupferman, R., 2009. Elastic theory of unconstrained non-Euclidean plates. J. Mech. Phys. Solids 57 (4), 762–775.

Ehlers, W., Markert, B., Röhrle, O., 2009. Computational continuum biomechanics with application to swelling media and growth phenomena. GAMM Mitt. 32 (2), 135–156.

Epstein, M., Maugin, G.A., 2000. Thermomechanics of volumetric growth in uniform bodies. Int. J. Plast. 16 (7), 951–978.

Ganghoffer, J.F., 2013. A kinematically and thermodynamically consistent volumetric growth model based on the stress-free configuration. Int. J. Solids Struct. 50 (20), 3446–3459.
Ganghoffer, J.F., Sokolowski, J., 2014. A micromechanical approach to volumetric and surface growth in the framework of shape optimization. Int. J. Eng. Sci. 74, 207–226.
Ganghoffer, J.F., Plotnikov, P.I., Sokołowski, J., 2014. Mathematical modeling of volumetric material growth in thermoelasticity. J. Elast., 1–28.
Garikipati, K., Arruda, E.M., Grosh, K., Narayanan, H., Calve, S., 2004. A continuum treatment of growth in biological tissue: the coupling of mass transport and mechanics. J. Mech. Phys. Solids 52 (7), 1595–1625.
Göktepe, S., Abilez, O.J., Kuhl, E., 2010a. A generic approach towards finite growth with examples of athlete's heart, cardiac dilation, and cardiac wall thickening. J. Mech. Phys. Solids 58 (10), 1661–1680.
Göktepe, S., Abilez, O.J., Parker, K.K., Kuhl, E., 2010b. A multiscale model for eccentric and concentric cardiac growth through sarcomerogenesis. J. Theor. Biol. 265 (3), 433–442.
Goriely, A., Vandiver, R., 2010. On the mechanical stability of growing arteries. IMA J. Appl. Math. 75 (4), 549–570.
Goriely, A., Robertson-Tessi, M., Tabor, M., Vandiver, R., 2008. Elastic growth models. In: Mondaini, R., Pardalos, P.M. (Eds.), Mathematical Modelling of Biosystems. Applied Optimization, vol. 12. Springer, Berlin Heidelberg, pp. 1–44.
Grillo, A., Federico, S., Wittum, G., 2012. Growth, mass transfer, and remodeling in fiber-reinforced, multi-constituent materials. Int. J. Nonlinear Mech. 47 (2), 388–401.
Gruttmann, F., Taylor, R.L., 1992. Theory and finite element formulation of rubberlike membrane shells using principal stretches. Int. J. Numer. Methods Eng. 35 (5), 1111–1126.
Himpel, G., Kuhl, E., Menzel, A., Steinmann, P., 2005. Computational modelling of isotropic multiplicative growth. Comput. Model. Eng. Sci. 8, 119–134.
Humphrey, J.D., 2003. Review paper: continuum biomechanics of soft biological tissues. Proc. R. Soc. Lond. A 459 (2029), 3–46.
Jones, G.W., Chapman, S.J., 2012. Modeling growth in biological materials. SIAM Rev. 54 (1), 52–118.
Kim, J., Hanna, J.A., Byun, M., Santangelo, C.D., Hayward, R.C., 2012. Designing responsive buckled surfaces by halftone gel lithography. Science 335 (6073), 1201–1205.
Klisch, S.M., Van Dyke, T.J., Hoger, A., 2001. A theory of volumetric growth for compressible elastic biological materials. Math. Mech. Solids 6 (6), 551–575.
Kröner, E., 1959. Allgemeine kontinuumstheorie der versetzungen und eigenspannungen. Arch. Ration. Mech. Anal. 4 (1), 273–334.
Kuhl, E., 2013. Growing matter: a review of growth in living systems. J. Mech. Behav. Biomed. Mater. 29, 529–543.
Kuhl, E., Steinmann, P., 2003. Theory and numerics of geometrically non-linear open system mechanics. Int. J. Numer. Methods Eng. 58 (11), 1593–1615.
Kuhl, E., Maas, R., Himpel, G., Menzel, A., 2007. Computational modeling of arterial wall growth. Biomech. Model. Mechanobiol. 6 (5), 321–331.
Lee, E.H., 1969. Elastic–plastic deformation at finite strains. J. Appl. Mech. 36, 1–6.
Li, B., Cao, Y.P., Feng, X.Q., 2011a. Growth and surface folding of esophageal mucosa: a biomechanical model. J. Biomech. 44 (1), 182–188.
Li, B., Jia, F., Cao, Y.P., Feng, X.Q., Gao, H., 2011b. Surface wrinkling patterns on a core–shell soft sphere. Phys. Rev. Lett. 106 (23), 234–301.
Liang, H., Mahadevan, L., 2009. The shape of a long leaf. Proc. Natl. Acad. Sci. 106 (52), 22049–22054.
Loret, B., Simões, F.M., 2005. A framework for deformation, generalized diffusion, mass transfer and growth in multi-species multi-phase biological tissues. Eur. J. Mech. A Solids 24 (5), 757–781.
Lubarda, V.A., 2004. Constitutive theories based on the multiplicative decomposition of deformation gradient: thermoelasticity, elastoplasticity, and biomechanics. Appl. Mech. Rev. 57 (2), 95–108.
Lubarda, V.A., Hoger, A., 2002. On the mechanics of solids with a growing mass. Int. J. Solids Struct. 39 (18), 4627–4664.
Maugin, G.A., Imatani, S., 2003. Material growth in solid-like materials. In: Miehe, C. (Ed.), IUTAM Symposium on Computational Mechanics of Solid Materials at Large Strains. Springer, Berlin Heidelberg, pp. 221–234.
Menzel, A., 2007. A fibre reorientation model for orthotropic multiplicative growth. Biomech. Model. Mechanobiol. 6 (5), 303–320.
Menzel, A., Kuhl, E., 2012. Frontiers in growth and remodeling. Mech. Res. Commun. 42, 1–14.
Narayanan, H., Arruda, E.M., Grosh, K., Garikipati, K., 2009. The micromechanics of fluid–solid interactions during growth in porous soft biological tissue. Biomech. Model. Mechanobiol. 8 (3), 167–181.
Reese, S., Wriggers, P., 1995. A finite element method for stability problems in finite elasticity. Int. J. Numer. Methods Eng. 38 (7), 1171–1200.
Rodriguez, E.K., Hoger, A., McCulloch, A.D., 1994. Stress-dependent finite growth in soft elastic tissues. J. Biomech. 27 (4), 455–467.
Stojanović, R., Djuric, S., Vujosevic, L., 1964. On finite thermal deformations. Arch. Mech. Stosow. 16, 103–108.
Taber, L.A., 1995. Biomechanics of growth, remodeling, and morphogenesis. Appl. Mech. Rev. 48, 487–545.
Vignes, C., Papadopoulos, P., 2010. Material growth in thermoelastic continua: theory, algorithmics, and simulation. Comput. Methods Appl. Mech. Eng. 199 (17), 979–996.
Wriggers, P., 2008. Nonlinear Finite Element Methods. Springer, Berlin Heidelberg.
Yavari, A., 2010. A geometric theory of growth mechanics. J. Nonlinear Sci. 20 (6), 781–830.
Yavari, A., 2013. Compatibility equations of nonlinear elasticity for non-simply-connected bodies. Arch. Ration. Mech. Anal. 209 (1), 237–253.
Yin, J., Chen, X., Sheinman, I., 2009. Anisotropic buckling patterns in spheroidal film/substrate systems and their implications in some natural and biological systems. J. Mech. Phys. Solids 57 (9), 1470–1484.
Zimmerman, J.A., Bammann, D.J., Gao, H., 2009. Deformation gradients for continuum mechanical analysis of atomistic simulations. Int. J. Solids Struct. 46 (2), 238–253.